Master's thesis

2019

Arne Valentin Espedal

NTNU
Norwegian University of
Science and Technology
Faculty of Natural Sciences
Department of Physics

Arne Valentin Espedal

Determination of collagen organization in cartilage by polarized second harmonic microscopy

June 2019

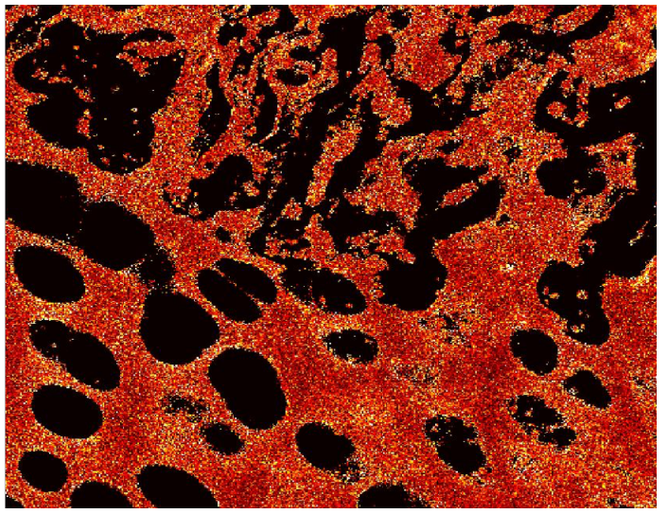

NTNU
Norwegian University of
Science and Technology

NTNU
Norwegian University of
Science and Technology

NTNU
Norwegian University of
Science and Technology

Determination of collagen organization in cartilage by polarized second harmonic microscopy

Arne Valentin Espedal

Applied Physics
Submission date: June 2019
Supervisor: Magnus Borstad Lilledahl

Norwegian University of Science and Technology
Department of Physics

Abstract

Cartilage is a connective tissue found in most joints in mammals. A main constituent of cartilage is fibrillar collagen which is present in the extracellular matrix. Determining collagen structures in cartilage is essential for early diagnosis of joint disorders such as osteochondrosis in both human medicine and the agriculture.

This thesis analyzes the possibility of determining collagen structures in cartilage by a nonlinear optical microscopy method known as polarized second harmonic generation. This is done by expanding a theoretical model of collagen fibril organization originally developed by Rouede et al [1] in order to simulate collagen structures in cartilage. Collagen structures were simulated with *a priori* known structural angles and compared to experimental data, with the purpose of correlating the data sets and determining the sub-resolution collagen structures of the samples.

Samples such as tendon, bone and cartilage were imaged. A main assumption is that collagen fibrils in cartilage are disordered, while fibrils in tendon are almost completely ordered. The collagen structure in tendon was successfully determined based on simulations, verifying the model.

However, polarized second harmonic microscopy proved unsuccessful at distinguishing between experimental data from bone, tendon and cartilage. Cartilage simulations of disordered fibrils did not correspond to measured data, implying that on scale of the optical point spread function of this experiment, collagen in cartilage is ordered.

Sammendrag

Brusk er et bindevev som finnes i de fleste ledd i pattedyr. En av de viktigste bestanddelene i brusk er kollagen og finnes i den ekstracellulære matrisen. Bestemmelse av kollagenstrukturer i brusk er viktig for tidlig diagnostisering av leddsykdommer som for eksempel osteochondrose i både medisin og innen landbruksnæringen.

Denne oppgaven analyserer muligheten for å bestemme kollagenstrukturer i brusk ved å bruke en ikke-lineær mikroskopimetode kjent som polarisert andre-harmonisk generasjon. Dette blir gjort ved å utvide en teoretisk modell av kollagenfibrilers strukturer utviket av Rouede et al [1] for å simulere brusk. Kollagenstrukturer ble simulert med *a priori* kjente strukturelle vinkler og sammenlignet med eksperimentelle data for å korrelere disse, og dermed bestemme kollagenstrukturer i bruskprøver.

Brusk, sener og bein ble avbildet. Det ble antatt at kollagenfibrilene i brusk er uordnet og at fibrilene i sener er nesten fullstendig ordnet. Simuleringer av sener var vellykket, hvilket bekrefter simuleringsmodellen.

Polarisert andre-harmonisk generasjonsmikroskopi viste seg å ikke kunne skille mellom eksperimentelle data fra bein, sener eller brusk. Brusksimuleringer viste seg heller ikke å korrespondere til målte data, hvilket indikerer at på nivået til den optiske punktspredningsfunksjonen til mikroskopet brukt i denne oppgaven er kollagenfibrilene i brusk ordnet.

Acknowledgements

I would like to thank my supervisor Magnus Borstad Lilledahl for his optimism and for always being available. Astrid Bjørkøy provided much-needed assistance with my experimental work. Above all I would like to thank my wife Xingyu for her love and everlasting support. This thesis would not be possible without her. Thank you.

Contents

Chapter 1

Introduction

1.1 Motivation

Collagen is the most common protein in humans, accounting for over 25% of the protein mass [2]. Diseases like bone cancer, liver fibrosis or cartilage degeneration are all caused by changes in collagen fibrillar organization.

Osteochondrosis is a common joint disorder that occurs in humans and animals such as pigs and horses [3]. By detecting changes in collagen structures within cartilage, osteochondrosis can be detected at an early stage, benefiting both human medicine and the agricultural industry.

This can possibly be done using a nonlinear optical phenomena called second harmonic microscopy (SHG). SHG is a nonlinear optical phenomena which is sensitive to the second order electric susceptibility of collagen fibrils [4]. Several models with various degrees of sophistication have been developed in order to determine collagen organization based on polarization dependent signals [5, 6, 7]. The latest model connecting the polarized SHG variations to collagen structure on a nanometric scale was developed in 2018 by Rouede et al [8] and has been shown to differentiate between various collagen tissues, including healthy and fibriotic rat livers. However, it has not been implemented and explored for cartilage.

By utilizing polarized SHG microscopy as a novel tool for analyzing collagen structures in cartilage, diseases such as osteochondrosis be diagnozed much earlier than by conventional methods.

1.2 Background

1.2.1 Collagen

Collagen is the most common protein found in the human body and currently 28 different types have been discovered [9]. Collagen molecules consist of three polypeptide chains, arranged in a triple helix structure called tropocollagen. Tropocollagen molecules form

fibrils through covalent cross-linking. These fibrils can be arranged in different ways and form bundles depending on the type of collagen. Two of the most common fibrillar collagen types are type I and type II collagen. Type II is mainly found along with proteoglycans in the extracellular matrix (ECM) in cartilage. The ECM is a network of molecules providing structural support surrounding cells [10]. Both type I and type II collagen molecules are periodically cross-striated fibrils [11].

The main difference between collagen types is that the triple helices consist of different peptide chains which leads to a difference in morphology on the fibrillar level.

1.2.2 Collagen Type I and II

Type I collagen consists of molecules forming fibrils with a diameter of 30-200nm [12]. These fibrils possess properties such as stronger tensile strength than steel and can be bundled on a micrometer scale length as is the case for tendon. It is also found in skin and is in general characterized by straight aligned and periodically cross-striated fibrils [10, 11].

Collagen type I is a heterotrimer formed by two identical $\alpha 1$(I)-chains and one $\alpha 2$(I)-chain. Similarly, collagen type II is a homotrimer formed by three identical $\alpha 1$(II) chains. In both cases, procollagen is then exposed to the enzyme procollagen peptidase, which removes the terminal peptides of the procollagen molecules forming tropocollagen. Tropocollagen molecules are then assembled into collagen fibrils, which form bundles organized in different ways depending on collagen type. For collagen type I, these fibrils are straight and aligned forming tissues like skin or tendon. For collagen type II, fibrils tend to be disordered as shown by scanning electron microscopy [13].

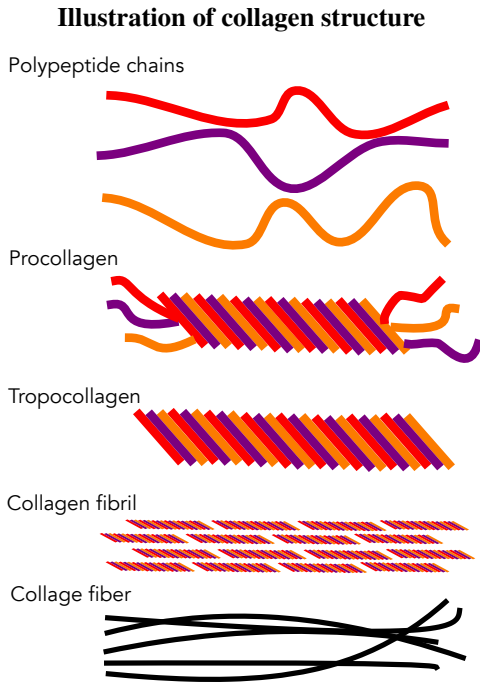

Figure 1.1: Illustraton of collagen structure. Three identical α1(II) chains (polypeptide chains) form tropocollagen for collagen type II. For collagen type I, two α1(I) and one α2(I) chain form tropocollagen. In both cases, tropocollagen self-assemble into collagen fibrils.

1.2.3 Collagen structure in cartilage

In cartilage, around 20% of the tissue surrounding the cells consist of collagen type II. Since collagen type II is characterized by disordered fibrils, cartilage is assumed to possess similar characteristics. The main assumption is that the subresolution polarization dependent SHG signals can be utilized to separate between collagen type II and type I and hence between cartilage and bone or tendon. The goal of this master thesis is the development of an existing model of collagen structure made by Rouede et al [1] based on *a priori* known structural information. It will be further developed in order to be used to distinguish between collagen types I and II and by extension cartilage from bone.

Chapter 2

Theory

2.1 Second harmonic generation

Second harmonic generation (SHG) is a nonlinear optical phenomena, often used for imaging biological structures, where according to quantum theory, two photons with frequency ω are combined and a single photon with frequency 2ω is emitted as shown in figure 2.1 [14]. It is a relatively weak effect, requiring high intensity lasers in order to detect a signal.

SHG requires non-centrosymmetric molecules, which means that the material cannot possess points of inversion symmetry. SHG requires a material to be ordered for the photon mixing to occur. The process is instantaneous and occurs as a consequence of the incoming light inducing a second-order polarization in the medium.

The second order polarization from a classical wave theory perspective is given by

$$P_{\mathrm{i}}^{(2)} = \sum_{\mathrm{jk}} \epsilon_0 \chi_{\mathrm{ijk}}^{(2)} E_{\mathrm{j}} E_{\mathrm{k}} \tag{2.1}$$

In this equation, ϵ_0 is the permittivity in vacuum. i, j and k are Cartesian coordinates. $\chi_{\mathrm{ijk}}^{(2)}$ is the second order susceptibility and describes the second-order polarization in a material when subjected to an applied electric field.

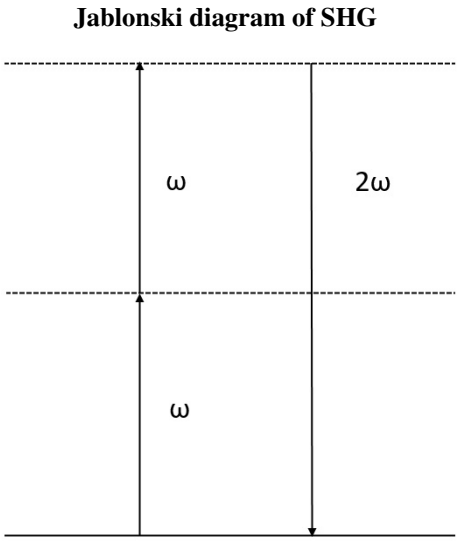

Figure 2.1: Jablonski diagram illustrating SHG. Two photons are converted and a single photon with twice the energy is emitted due to second harmonic fluctuation of the dipole moment.

2.2 Symmetry

In general for three wave-mixing processes, there are 3x3x3 = 27 elements in the nonlinear susceptibility tensor. For a three-wave process in general, two waves, ω_1 and ω_2 interact to form a third wave, $\omega_3 = \omega_1 + \omega_2$.

The polarization can be expressed as

$$P_{\mathrm{i}}(\omega_1 + \omega_2) = \sum_{\mathrm{jk}} \chi^{(2)}_{\mathrm{ijk}}(\omega_1, \omega_2) E_{\mathrm{j}}(\omega_1) E_{\mathrm{k}}(\omega_2) \tag{2.2}$$

2.2.1 Degenerate case symmetry

The tensor reduces to 18 elements due the fact that for SHG, $\omega_1 = \omega_2 = \omega$ is an inherent property. Inserted into equation 2.2, it is evident that

$$\chi^{(2)}_{\mathrm{ijk}}(\omega, \omega) = \chi^{(2)}_{\mathrm{ikj}}(\omega, \omega) \tag{2.3}$$

The nonlinear susceptibility tensor can be written as illustrated in equation 2.4 with 18 elements. This is due to the symmetry in equation 2.3 as 9 of the 27 elements are no longer independent.

$$\chi^{(2)} = \begin{bmatrix} \chi^{(2)}_{11} & \chi^{(2)}_{12} & \chi^{(2)}_{13} & \chi^{(2)}_{14} & \chi^{(2)}_{15} & \chi^{(2)}_{16} \\ \chi^{(2)}_{21} & \chi^{(2)}_{22} & \chi^{(2)}_{23} & \chi^{(2)}_{24} & \chi^{(2)}_{25} & \chi^{(2)}_{26} \\ \chi^{(2)}_{31} & \chi^{(2)}_{32} & \chi^{(2)}_{33} & \chi^{(2)}_{34} & \chi^{(2)}_{35} & \chi^{(2)}_{36} \end{bmatrix} \tag{2.4}$$

Here, $x = 1, y = 2, z = 3$ and contracted notation is used for the two last indices of $\chi^{(2)}_{\mathrm{ijk}}$: $xx = 1, yy = 2, zz = 3, zy = yz = 4, zx = xz = 5$ and $yx = xy = 6$.

2.2.2 Kleinman's symmetry

Kleinman's symmetry states that in a material, far away from any resonances and in the absence of strong dispersion, interchanged tensor components are independent of frequency;

$$\chi^{(2)}_{\mathrm{ijk}}(\omega_1, \omega_2) \cong \chi^{(2)}_{\mathrm{ijk}} \tag{2.5}$$

This means that all frequency arguments can be interchanged between the susceptibility tensor elements, which leads to the following relations [15]

$$\begin{gathered}\chi^{(2)}_{\mathrm{ijk}}(\omega = \omega_1 + \omega_2) = \chi^{(2)}_{\mathrm{jki}}(\omega_1 = -\omega + \omega_2) = \chi^{(2)}_{\mathrm{kij}}(\omega_2 = \omega - \omega_2) = \\ \chi^{(2)}_{\mathrm{ikj}}(\omega = \omega_2 + \omega_1) = \chi^{(2)}_{\mathrm{jik}}(\omega_1 = \omega_2 - \omega) = \chi^{(2)}_{\mathrm{kji}}(\omega_2 = -\omega_2 + \omega)\end{gathered} \tag{2.6}$$

As shown in equation 2.5, the tensor elements are independent of frequency, hence the indices can be permuted as in equation 2.6 without permuting the frequencies. This leads to the following symmetries [16, 17].

$$\chi^{(2)}_{\mathrm{ijk}} = \chi^{(2)}_{\mathrm{ikj}} = \chi^{(2)}_{\mathrm{jki}} = \chi^{(2)}_{\mathrm{kij}} = \chi^{(2)}_{\mathrm{kji}} = \chi^{(2)}_{\mathrm{jik}} \tag{2.7}$$

Hence the matrix is reduced to 10 independent elements and is given by

$$\chi^{(2)} = \begin{bmatrix} \chi^{(2)}_{11} & \chi^{(2)}_{12} & \chi^{(2)}_{13} & \chi^{(2)}_{14} & \boldsymbol{\chi^{(2)}_{31}} & \boldsymbol{\chi^{(2)}_{21}} \\ \chi^{(2)}_{21} & \chi^{(2)}_{22} & \chi^{(2)}_{23} & \boldsymbol{\chi^{(2)}_{32}} & \boldsymbol{\chi^{(2)}_{14}} & \boldsymbol{\chi^{(2)}_{12}} \\ \chi^{(2)}_{31} & \chi^{(2)}_{32} & \chi^{(2)}_{33} & \boldsymbol{\chi^{(2)}_{23}} & \boldsymbol{\chi^{(2)}_{13}} & \boldsymbol{\chi^{(2)}_{14}} \end{bmatrix} \tag{2.8}$$

where bolded elements are dependent.

2.2.3 Cylindrical symmetry

The susceptibility tensor can be even further simplified by assuming cylindrical symmetry in the specimen. In general, rotating a coordinate system from x', y', z' to x, y, z, yields the following susceptibility tensor;

$$\chi^{(2)}_{\mathrm{ijk}} = \sum_{\mathrm{i'j'k'}} \cos\theta_{\mathrm{ii'}} \cos\theta_{\mathrm{jj'}} \cos\theta_{\mathrm{kk'}} \chi^{(2)}_{\mathrm{i'j'k'}} \tag{2.9}$$

If invariance under rotation in the xy-plane (i.e. cylindrical symmetry) is assumed, all tensor elements in equation 2.8 vanish except for the following due to none of indices i,j,k involving z. [17]:

$$
\begin{aligned}
\chi^{(2)}_{\mathrm{zzz}} &= \chi^{(2)}_{33} \\
\chi^{(2)}_{\mathrm{zxx}} &= \chi^{(2)}_{\mathrm{zyy}} = \chi^{(2)}_{31} \\
\chi^{(2)}_{\mathrm{xxz}} &= \chi^{(2)}_{\mathrm{xzx}} = \chi^{(2)}_{\mathrm{yyz}} = \chi^{(2)}_{\mathrm{yzy}} = \chi^{(2)}_{15} \\
\chi^{(2)}_{\mathrm{xyz}} &= \chi^{(2)}_{\mathrm{xzy}} = -\chi^{(2)}_{\mathrm{yxz}} = -\chi^{(2)}_{\mathrm{yzx}} = \chi^{(2)}_{14}
\end{aligned}
\tag{2.10}
$$

Which leads to the remaining susceptibility tensor being given by

$$
\chi^{(2)} = \begin{bmatrix}
0 & 0 & 0 & \chi^{(2)}_{14} & \chi^{(\mathbf{2})}_{\mathbf{31}} & 0 \\
0 & 0 & 0 & \chi^{(\mathbf{2})}_{\mathbf{31}} & \chi^{(\mathbf{2})}_{\mathbf{14}} & 0 \\
\chi^{(2)}_{31} & \chi^{(\mathbf{2})}_{\mathbf{31}} & \chi^{(2)}_{33} & 0 & 0 & \chi^{(\mathbf{2})}_{\mathbf{14}}
\end{bmatrix}
\tag{2.11}
$$

2.2.4 Single-axis symmetry

There exists one final simplification for the second order susceptibility tensor if the molecules are structures as helices. If molecules are organized, each with some x', y', z' relative to the bulk axes of several molecules x, y, z,

$$
\chi^{(2)}_{\mathrm{ijk}} = \sum_{\mathrm{i'j'k'}} \langle \cos\theta_{\mathrm{ii'}} \cos\theta_{\mathrm{jj'}} \cos\theta_{\mathrm{kk'}} \rangle \beta_{\mathrm{i'j'k'}}
\tag{2.12}
$$

where β represents hyperpolarizability and is assumed to be a constant in the $z'z'z'$ axis only, giving $\beta_{\mathrm{i'j'k'}} = \beta$. The brackets represent averaging over all molecules. In addition, $\theta_{\mathrm{zz'}}$ is assumed to be a constant angle for all molecules and ϕ is random for each molecule. Using these assumptions, the four remaining tensor elements can then be calculated as follows

$$
\begin{aligned}
\chi^{(2)}_{\mathrm{zzz}} &= \chi^{(2)}_{33} = N\cos\theta^3\beta \\
\chi^{(2)}_{\mathrm{zxx}} &= \chi^{(2)}_{31} = \frac{N}{2}\cos\theta^2\beta \\
\chi^{(2)}_{\mathrm{xxz}} &= \chi^{(2)}_{15} = N\cos\theta\sin\theta^2\langle\sin\phi^2\rangle\beta = \frac{N}{2}\cos\theta^2\beta \\
\chi^{(2)}_{\mathrm{xyz}} &= \chi^{(2)}_{14} = N\cos\theta\sin\theta^2\langle\cos\phi\sin\phi\rangle\beta = 0
\end{aligned}
\tag{2.13}
$$

where N is the number of molecules. Since two of the elements clearly are not independent, this leads to a remaining two independent second order susceptibility tensor elements.

After considering all symmetries, the tensor in equation 2.4 simplifies to

$$\chi_{\mathrm{ijk}} = \begin{bmatrix} 0 & 0 & 0 & 0 & \boldsymbol{\chi_{31}} & 0 \\ 0 & 0 & 0 & \chi_{31} & 0 & 0 \\ \boldsymbol{\chi_{31}} & \boldsymbol{\chi_{31}} & \chi_{33} & 0 & 0 & 0 \end{bmatrix} \tag{2.14}$$

where the second order subscript has been neglected for simplicity. Thus, there are only two independent second order susceptibility tensor elements for collagen.

2.2.5 Second harmonic generation intensity

The reduction of the second order susceptibility tensor into two independent elements, results in a simplified matrix equation for the second order polarization given by equation 2.1 and expanded below

$$\begin{bmatrix} P_{\mathrm{x}}^{2\omega} \\ P_{\mathrm{y}}^{2\omega} \\ P_{\mathrm{z}}^{2\omega} \end{bmatrix} = \epsilon_0 \begin{bmatrix} 0 & 0 & 0 & 0 & 0 & 0 \\ 0 & 0 & 0 & \chi_{31} & 0 & 0 \\ 0 & \chi_{31} & \chi_{33} & 0 & 0 & 0 \end{bmatrix} \begin{bmatrix} E_{\mathrm{x}}^2 \\ E_{\mathrm{y}}^2 \\ E_{\mathrm{z}}^2 \\ 2E_{\mathrm{y}}E_{\mathrm{z}} \\ 2E_{\mathrm{x}}E_{\mathrm{z}} \\ 2E_{\mathrm{x}}E_{\mathrm{y}} \end{bmatrix} \tag{2.15}$$

Which explicitly calculated leads to the following expressions for the polarization components

$$\begin{aligned} P_{\mathrm{x}}^{2\omega} &= 0 \\ P_{\mathrm{y}}^{2\omega} &= 2\epsilon_0 \chi_{15}^{(2)} E_{\mathrm{y}}^{\omega} E_{\mathrm{z}}^{\omega} \\ P_{\mathrm{z}}^{2\omega} &= \epsilon_0 [\chi_{31}^{(2)} (E_{\mathrm{y}}^{\omega})^2 + \chi_{33}^{(2)} (E_{\mathrm{z}}^{\omega})^2] \end{aligned} \tag{2.16}$$

.

The SHG intensity $I^{2\omega} \propto [(P_{\mathrm{y}}^{2\omega})^2 + (P_{\mathrm{z}}^{2\omega})^2]$ is calculated from equation 2.16 by using $E_{\mathrm{y}}^{\omega} \propto \sin(\alpha - \gamma)$ and $E_{\mathrm{z}}^{\omega} \propto \cos(\alpha - \gamma)$where $(\alpha - \gamma)$ is the angle of polarization of the incoming electrical field relative to the long axis of the cylinder (or z-axis of the molecule) in the image plane. This leads to the following expression for SHG intensity

$$I^{2\omega} = c(\chi_{31}^{(2)} \sin^2 2(\alpha - \gamma) + (\chi_{31}^{(2)} \sin^2(\alpha - \gamma) + \chi_{33}^{(2)} \cos^2(\alpha - \gamma))^2) \tag{2.17}$$

2.3 Method of linear least squares

In order to extract information about collagen organization through P-SHG, a method of curve-fitting equation 2.17 to the measured signal is required. There are several ways of doing this, one being through Fourier transforms [18]. Another linear least squares method for curve-fitting, proposed by Rouede et al [19], will be presented.

Equation 2.17 can be rewritten as

$$I^{\mathrm{th}} = A + B\cos 2(\gamma - \alpha) + C\cos(\gamma - \alpha) \tag{2.18}$$

where

$$\begin{aligned} A &= c(4 + 3a^2 + 3b^2 + 2ab)/8 \\ B &= c(4b^2 - 4a^2)/8 \\ C &= c(a^2 + b^2 - 2ab - 4)/16 \end{aligned}$$

by using the following trigonometric identities

$$\begin{aligned} a'^2\cos x + b'^2\sin x &= \frac{1}{2}(a'^2 + b'^2 + (a' - b')\cos 2x) \\ \cos x^2 &= \frac{1}{2}(1 + \cos 2x) \\ \sin x^2 &= \frac{1}{2}(1 - \cos 2x) \end{aligned}$$

where a', b' and x are some arbitrary constants. a, b and c are constants given in equation 2.17. Notice that I^{th} represents a theoretical polarization dependent intensity curve.

Then by applying the following trigonometric addition formula

$$\cos(\gamma - \alpha) = \cos\gamma\cos\alpha - \sin\gamma\sin\alpha$$

Equation 2.18 simplifies to

$$I^{\mathrm{th}} = C_1 + C_2\cos 2\alpha + C_3\sin 2\alpha + C_4\cos 4\alpha + C_5\sin 4\alpha \tag{2.19}$$

where

$$\begin{aligned} C_1 &= A = c(4 + 3a^3 + 3b^2 + 2ab)/8 \\ C_2 &= B\cos 2\gamma = c(4b^2 - 4a^2)/8\cos 2\gamma \\ C_3 &= B\sin 2\gamma = c(4b^2 - 4a^2)/8\sin 2\gamma \\ C_4 &= C\cos 4\gamma = c(a^2 + b^2 - 2ab - 4)/8\cos 4\gamma \\ C_5 &= C\sin 4\gamma = c(a^2 + b^2 - 2ab - 4)/8\sin 4\gamma \end{aligned} \tag{2.20}$$

In order to solve equation 2.19, the equation can be written in matrix form as

$$\mathbf{I} = A\mathbf{C} \tag{2.21}$$

where

$$\mathbf{I}^{\mathrm{th}} = \begin{bmatrix} I^{\mathrm{th}} \\ \vdots \\ I_i^{\mathrm{th}} \\ \vdots \\ I_N^{\mathrm{th}} \end{bmatrix} A = \begin{bmatrix} 1 & \cos 2\alpha_1 & \sin 2\alpha_1 & \cos 4\alpha_1 & \sin 4\alpha_1 \\ \vdots & \vdots & \vdots & \vdots & \vdots \\ 1 & \cos 2\alpha_i & \sin 2\alpha_i & \cos 4\alpha_i & \sin 4\alpha_i \\ \vdots & \vdots & \vdots & \vdots & \vdots \\ 1 & \cos 2\alpha_N & \sin 2\alpha_N & \cos 4\alpha_N & \sin 4\alpha_N \end{bmatrix} \mathbf{C} = \begin{bmatrix} C_1 \\ \vdots \\ \vdots \\ \vdots \\ C_5 \end{bmatrix} \tag{2.22}$$

with α_i uniformly distributed between 0° and 180° with N number of increments.

The coefficients $C_1 ... C_5$ can then be estimated by solving the following least linear squares problem

$$\mathbf{C}_{\mathrm{estimate}} = \arg\min_{\mathrm{c}} \sum_{i=1}^{N} \left| I^{\exp}(\alpha_i) - I^{\mathrm{th}}(\alpha_i) \right|^2 = \arg\min_{\mathrm{c}} \left| \mathbf{I}^{\exp} - A\mathbf{C} \right|^2 \tag{2.23}$$

The solution can be written as

$$C_{\mathrm{estimate}} = (A^T A)^{-1} A^T \, \mathbf{I}^{\exp} \tag{2.24}$$

In order to solve for a and b, the solution to equation 2.24 is inserted into equation 2.20. To simplify, two coefficients R_1 and R_2 can be defined as follows

$$\begin{aligned} R_1 &= \sqrt{\frac{C_2^2 + C_3^2}{C_1^2}} = \sqrt{\frac{(4b^2 - 4a^2)^2}{4 + 3a^2 + 3b^2 + 2ab)^2}} \\ R_2 &= \sqrt{\frac{C_4^2 + C_5^2}{C_1^2}} = \sqrt{\frac{(a^2 + b^2 - 2ab - 4)^2}{4 + 3a^2 + 3b^2 + 2ab)^2}} \end{aligned} \tag{2.25}$$

By assuming that collagen possesses the special case of $a, b \in [0, 2]$ and with $a < b$ [18], R_1 and R_2 simplifies to

$$\begin{aligned} R_1 &= \frac{4\left|b^2 - a^2\right|}{4 + 3a^2 + 3b^2 + 2ab} \\ R_2 &= \frac{4 - (a - b)^2}{4 + 3a^2 + 3b^2 + 2ab} \end{aligned} \tag{2.26}$$

These expressions then lead to the following equations for factors a and b

$$\begin{aligned} a &= \sqrt{2}\sqrt{\frac{1 + R_2}{1 - R_2 - R_1} - \sqrt{\frac{1 - R_2 + R_1}{1 - R_2 - R_1}}} \\ b &= \sqrt{2}\sqrt{\frac{1 + R_2}{1 - R_2 + R_1} - \sqrt{\frac{1 - R_2 - R_1}{1 - R_2 + R_1}}} \end{aligned} \tag{2.27}$$

Since a and b corresponds to χ_{31}/χ_{15} and χ_{33}/χ_{15} respectively, this procedure can be implemented and run for each pixel each with N polarization angles in order to obtain $\rho = \chi_{33}/\chi_{31}$ for each pixel of an image.

Chapter 3

Model

In this chapter, a theoretical model for describing collagen structure through a hierarchy of levels is presented. Nonlinear susceptibilities are calculated based on these structures. The purpose of the model is the correlation of *a priori* calculated intensity SHG curves to measured intensity curves from real samples and subsequently establishing how a collagen sample is structured by comparison.

3.1 Theoretical model of collagen

The collagen fibrillar structure can be considered to be hierarchical with four distinct structural levels [20]. The first level is characterized by polypeptide chains forming a helices, see section 1.2.1. As can be seen in figure 3.1, angles (θ_H, ϕ_H) represent the polar and azimuthal helical angles for the helices. The second level in the hierarchical description of the collagen structure consists of triple helices composed of single helix polypeptide chains. Angles (θ_{3H}, ϕ_{3H}) represent analogous helical angles for the triple helix. The third level consists of these triple helices coiling around their own axes forming supercoiled fibrils with angles $(\theta_{SC}, \phi_{SC}$. The fourth level describes tilting of the fibril in the microscope stage with angles $\theta_T, \phi_T)$. These four levels constitute a hierarchical description of collagen fibrillar organization.

3.1.1 Nonlinear susceptibility of collagen

Collagen is non-centrosymmetric and is modeled as being cylindrically symmetric on the fibrillar level [21]. Thus it fullfills the requirements presented in chapter 2 for generating second harmonic signals. In addition, the nonlinear susceptibility tensor of collagen is simplified to two elements due to the presence of Kleinman symmetry and the initial assumption of cylindrical symmetry.

As the SHG signal is governed by the second order polarization of the collagen sample and thus the nonlinear susceptibility, a model for relating structural information to susceptibility is required. Equation 3.1 is such a model developed by Rouede et al [1].

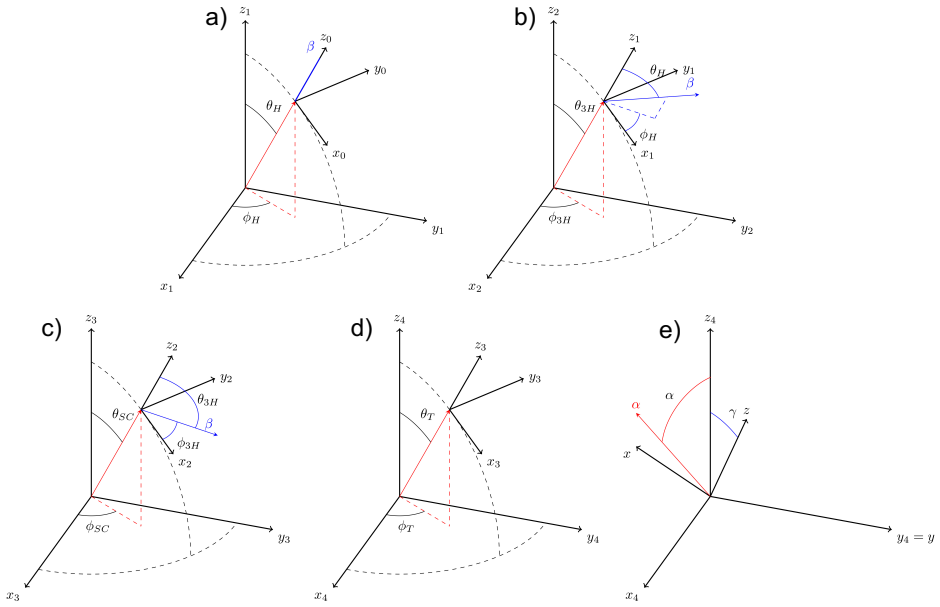

Figure 3.1: Figure showing the coordinate transformation between the four different hierarchical levels of the collagen model. a) Illustrates the transformation from the lowest level with coordinate system (x_0, y_0, z_0) to the helix-level with coordinates (x_1, y_1, z_1) and angles (θ_H,ϕ_H). The hyperpolarizability vector β is aligned with the z_0-axis. b) is a similar transformation to the triple-helix level with coordinate system (x_2, y_2, z_2) and triple helix angles (θ_{3H},ϕ_{3H}). c) shows the transformation to the supercoil level with coordinate system (x_3, y_3, z_3) and angles (θ_{SC},ϕ_{SC}). Finally, d) illustrates the transformation which represents the tilting of fibrils in the coordinate system (x_4, y_4, z_4) with angles (θ_T,ϕ_T). e) shows the polarization angle α of the incident laser beam and the effective orientation angle γ. $(x, y_4 = y, z)$ represent the coordinates of the microscope stage.

$$\begin{bmatrix} \chi_{33} \\ \chi_{31} = \chi_{15} \end{bmatrix} = \cos\theta_T \cos\theta_{SC} \cos\theta_{3H} \cos\theta_H \begin{bmatrix} \cos^2\theta_T & 3\sin^2\theta_T \\ \cos^2\phi_T \sin^2\theta_T & 1 - 3\cos^2\phi_T \sin^2\theta_T \end{bmatrix} \cdot \begin{bmatrix} \cos^2\theta_{SC} & 3\sin^2\theta_{SC} \\ \langle\cos^2\phi_{SC}\rangle \sin^2\theta_{SC} & 1 - 3\langle\cos^2\phi_{SC}\rangle \sin^2\theta_{SC} \end{bmatrix} \begin{bmatrix} \cos^2\theta_{3H} & 3\sin^2\theta_{3H} \\ \frac{1}{2}\sin^2\theta_{3H} & 1 - \frac{3}{2}\sin^2\theta_{3H} \end{bmatrix} \cdot \begin{bmatrix} \cos^2\theta_H & 3\sin^2\theta_H \\ \frac{1}{2}\sin^2\theta_H & 1 - \frac{3}{2}\sin^2\theta_H \end{bmatrix} \begin{bmatrix} \beta \\ 0 \end{bmatrix} \tag{3.1}$$

Equation 3.1 is a matrix equation describing how the second order susceptibility tensor elements are calculated. θ_H, θ_{3H}, θ_{SC} and θ_T represent polar angles of respectively the helix, triple helix, supercoil and tilt hierarchical levels. ϕ_{SC} and ϕ_T are the azimuthal angles of the supercoil and tilt hierarchical levels. Each matrix represents a euler rotation matrix to the higher hierarchical coordinate system, shown in figure 3.1.

3.1.2 Comparison with experimental values

A method of calculating the second order susceptibility of collagen fibrils based on their helical and fibrillar angles has been presented. This can be used to calculate a parameter ρ_{th} (theoretical ρ without application of noise) as a function of structural angles for each pixel of an image, providing a distribution of values.

3.1.3 Shot noise

In order to further develop the theoretical model, noise is considered. As the detected signal when imaging through SHG microscopy is weak, significant shot noise can be present. This can be minimized by increasing the signal strength when imaging, but can also be modeled by a Poisson process.

Using equation 2.17, a theoretical intensity contribution can be calculated for each pixel of an image as a function of the polarization angle of the incoming light. Poisson shot noise can then be added for each intensity curve. Furthermore, by fitting the noise-rendered intensity curves to equation 2.17, a new parameter ρ_{noise} can be calculated for each pixel, further improving correlation with experimental data.

Chapter 4

Methods

The following chapter consists of two parts, namely simulations and the experimental setup. First, simulations for creating a catalogue of $\rho_{\mathrm{th,noise}}$-distributions for *a priori* known helical angles, coil and tilt angles is elaborated upon. Then, the experimental setup and method used for acquiring analogous distributions, ρ_{exp}, for collagen-rich samples is presented. The main purpose is giving the reader an overview of how the simulations are run and how experimental data was collected. All code used is given in the appendix.

4.1 Simulation

The simulation of the theoretical model for collagen organization is presented in the following section. Figure 4.1 illustrates a few pixels for four given simulations. As can be seen in the top left, each pixel represents a fibril with a given tilt angle θ_{T}. Similarly, in the top right, each pixel represents a fibril with a different tilt angle. The total angular distribution is modelled either as normal distributions for various standard deviations or as a uniform distribution. The bottom row represents undulating fibrils with coil angle θ_{SC} for either fixed coil angle on the bottom right and variable coil angle on the bottom right.

4.1.1 Generation of angles

Gaussian distributions for angles (θ_H, θ_{3H}, θ_{SC}, θ_T, ϕ_T, ϕ_{SC}) with specified mean and standard deviance values were generated in Matlab [22]. Each azimuthal angle, ϕ_T, ϕ_{SC}, was allowed to be randomly distributed as they are of no consequence to the measured signal. The helical angles $\theta_{H,3H}$ were simulated as normal distributions with mean values and standard deviations $53° \pm 1°$ and $12° \pm 2°$ respectively for all simulations as found by Rouede et al [1]. In addition, angles were also simulated as uniform distributions in an attempt to simulate cartilage.

These angle distributions simulate the various collagen structures mentioned in chapter 1.2.1.

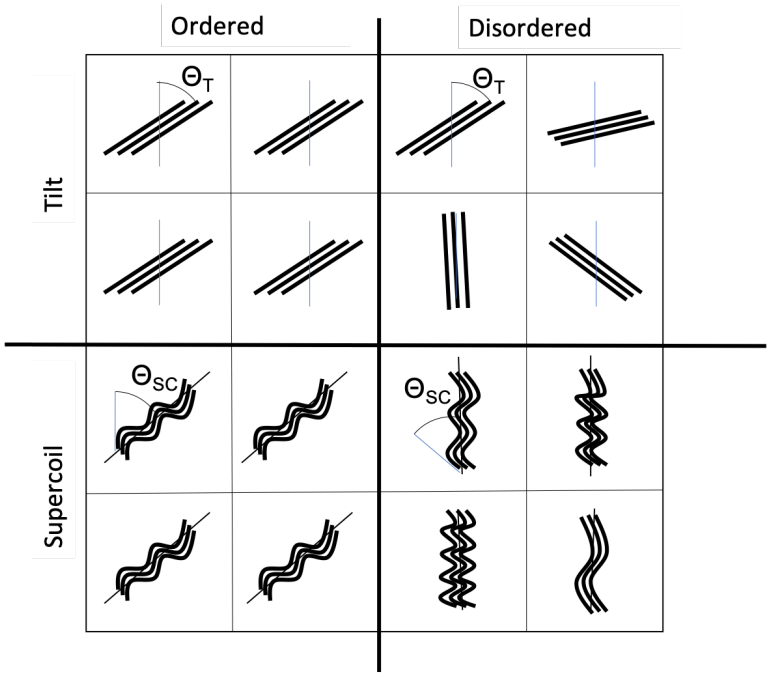

Figure 4.1: Illustration of simulated pixels for four cases. **(Top left)** Simulation with ordered fibrils with tilt angle θ_{T}. **(Top right)** Disordered fibrils. Each pixel is characterized by a fibril with a different tilt angle. **(Bottom left)** Undulating fibrils with a coil angle θ_{SC} as indicated. **(Bottom right)** Each pixel represents a fibril with a different coil angle. In addition, these cases are combined with disorder in both supercoil and tilt angles. Recreated and adapted from [8].

4.1.2 Simulation of susceptibility tensor

The generated angles for each pixel were used as input for the matrix equation given in equation 3.1 tensor elements, χ_{33}, χ_{31} and values $\rho_{\text{th}} = \chi_{33}/\chi_{31}$ were calculated for each of the 512×512 data points.

A simulation of ρ_{th} with variation of the input tilt angle θ_T is shown in figure 4.3a.

4.1.3 Application of shot noise

For real data acquisition there is shot noise present to some extent and it does affect the mean value of ρ-distributions. In order to provide better fit simulated data to experimental data, noise can be added.

For each generated array, the ρ_{th} distribution was inserted into equation 2.17 and a theoretical intensity contribution curve was generated for each pixel as a function of polarization angle. It was then rendered noisy by application of Poisson noise to each pixel's polarization-dependent curve. Figure 4.2 illustrates the application of shot noise to an arbitrary pixel's intensity curve.

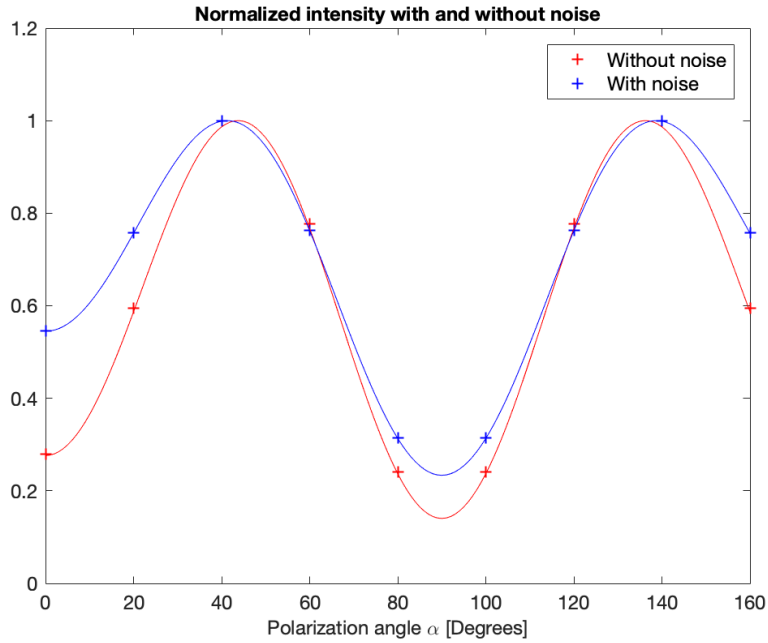

Figure 4.2: Intensity curve as a function of polarization with curve-fitting is shown for an arbitrary pixel for a given simulation. Simulation with and without added Poisson shot noise is illustrated. Note that both curves have been normalized.

A Least linear squares method developed by Rouede et al [19] and derived in section 2.3 was utilized in order to calculate new ρ_{noise} values by curve-fitting the noisy intensity

curves to equation 2.17.

Figure 4.3a illustrates simulations with and without noise applied. The histograms are in agreement with calculated distributions found by Rouede et al [8]. The model's capabilities were investigated by simulating variations in both θ_T and θ_{SC}.

In summary, an array of noise-rendered ρ_{noise} values have been created from an array of theoretical ρ_{th} simulated from *a priori* known angular distributions.

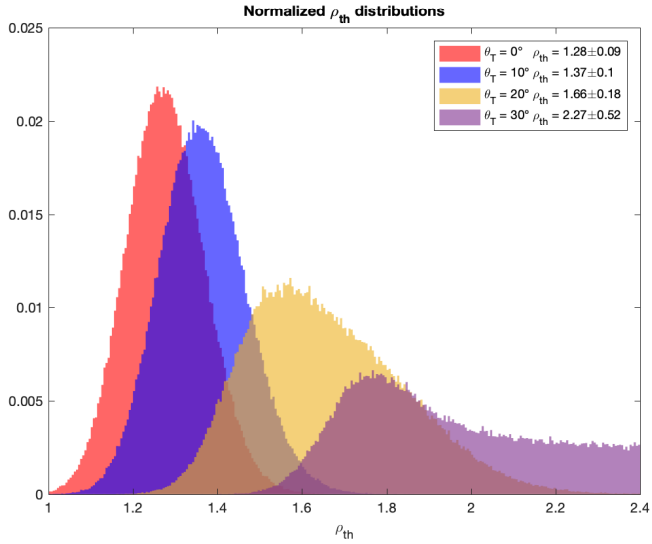

(a) Distribution of ρ_{th}

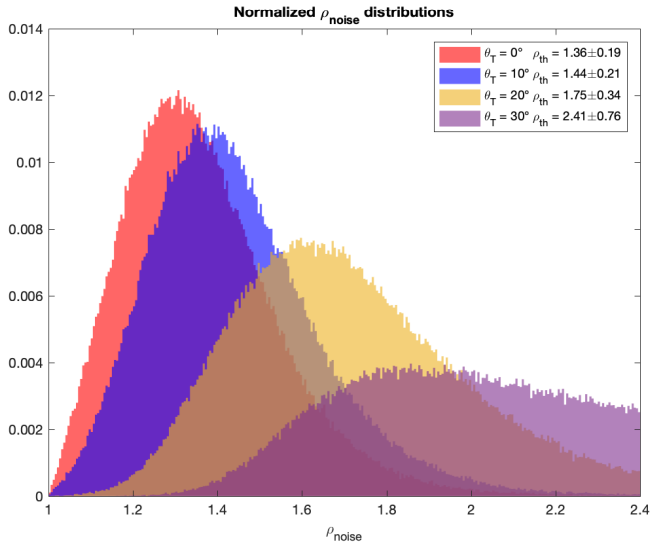

(b) Distribution of ρ_{noise}

Figure 4.3: $(\mathbf{a})$ Normalized histograms of ρ_{th} with helix angle $\theta_{\mathrm{H}} = 53 \pm 1°$, triple helix angle $\theta_{3\mathrm{H}} = 12 \pm 2°$ and tilt angles from $0°$ to $30°$ with $10°$ increments. $(\mathbf{b})$ Parameters as in $(\mathbf{a})$ with noise.

4.2 Instrumentation

4.2.1 Imaging system

Images were collected by a TCS SP8 confocal microscope produced by Leica and combined with a Chameleon Vision-S Ti:Sapphire laser tuned to a wavelength of $890\,\mathrm{nm}$. A HCX IRAPO L 25 x 0.95 WATER objective was used for all images. Reflected SHG was collected using a HyD-detector combined with a 435-455 bandpass filter. Forward SHG was also collected using a photon multiplier tube detector (PMT). The system is illustrated in figure 4.4. In addition the microscope was programmed to perform a tile scan using a HC PL APO 10x 0.40 DRY objective in order to create overview pictures of samples.

4.2.2 Polarization system

The incident laser beam was polarized by using a system composed by a polarizer, a quarter wave plate (AQWP10M-980 , Thorlabs) and a half wave plate (AHWP10M-980, Thorlabs). These plates were then rotated to a pair of fixed angles for each of the 9 desired polarization angles between $0°$ and 160° with 20° increments. An image consisting of 512×512 pixels with a resolution of $910\,\mathrm{nm} \times 910\,\mathrm{nm}$ was produced for each of the 9 polarization angles. The measurements were then calibrated post-imaging to account for intensity variations caused by the polarization setup.

4.3 Samples

Two kinds of samples were examined in this thesis; tendon from a gallus domesticus (chicken) and a knee joint from a sus scrofa (pig). The samples were obtained and prepared in conjunction with previous research [23].

4.3.1 Gallus domesticus

The two chicken samples were obtained from the knee joint of a commercially available chicken, and cut into two strips of about $50\,\mu\mathrm{m}$ thick at angles 20° and 30° relative to their long axes before being mounted on a coverslip with glycerol.

4.3.2 Sus scrofa

The pig samples originate from the right distal femur or knee joint of a pig. The right distal femur was fixed in 4% phosphate-buffered formaldehyde for more than 48 hours. A plug containing subchondral bone, cartilage and part of the tendon connected to the distal femur was obtained using a trephine. The plug was then decalcified in 10% EDTA and cut slices perpendicular to the articular surface. A vibratome was used to section one of the pieces into three $50\,\mu\mathrm{m}$ thick slices before they were mounted in glycerol on coverslips.

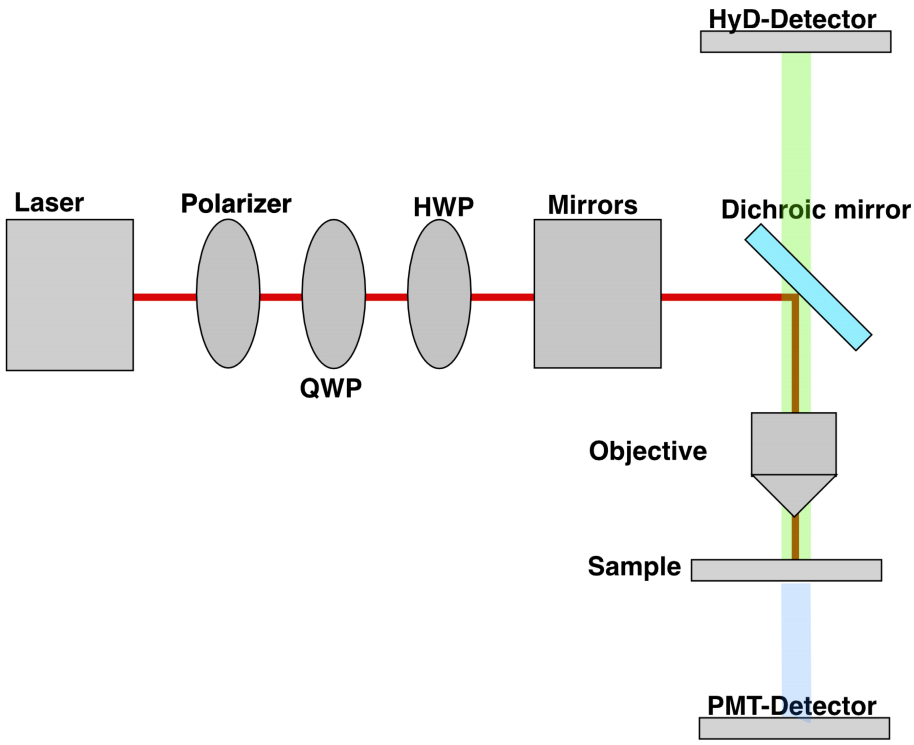

Figure 4.4: Simplified schematic drawing of LEICA SP8 with detectors and polarization setup. A chameleon Vision-S Ti:Sapphire laser tuned to 890nm is polarized through a polarizer (model) and then phase shifted through a quarter wave plate (QWP) and a half wave plate (HWP). The laser is scanned across the sample using galvanic mirrors, through a dichroic mirror into a HCX IRAPO L 25 x 0.95 WATER objective. SHG in the backwards direction is detected by a photon counting (HyD) detector and SHG in the forward direction is detected by a photon multiplier tube (PMT) detector.

4.4 Imaging

4.4.1 Chicken tendon

Sections of both chicken samples were imaged for each polarization angle between 0° to 160° with 20° increments using a 25X WATER objective with a scanning speed of 100Hz. The samples were all imaged on a relatively shallow depth of approximately $10\,\mu\mathrm{m}$ and signal was collected in the reflected direction. The nine polarization-dependant images were then overlaid forming an image with an intensity range of 0-2295. A threshold value of 200 was chosen and any pixels below this value were removed from the data set. The resulting intensity curves for each pixel were then used in order to calculate ρ_{exp} and main angle γ through the curve-fitting described in section 2.3, resulting in images with a resolution of 512×512 pixels over an area of $465\,\mu\mathrm{m} \times 465\,\mu\mathrm{m}$.

4.4.2 Distal femur of pig

A similar process as in section 4.4.1 was applied on the pig knee joint sample. A main difference is that the signal was also collected in the forward direction using the PMT-detector and the threshold value was set to 200 when processing due to lower overall signal from the cartilage sections.

Overview image

The microscope was programmed to section the distal femur sample into a grid consisting of approximately 130 tiles, covering the entire sample through using the 10X AIR objective. All tiles were imaged and later combined into one overview picture of the distal femur at 5474×5925 pixels with a total image size of $12.43\,\mathrm{mm} \times 13.45\,\mathrm{mm}$.

Chapter 5

Results

In this chapter, both simulated and experimental results are presented.

5.1 Simulation of tilt and supercoil angle distributions

All simulations were performed with helical angles θ_H and θ_{3H} modeled as Gaussian distributions as described in section 4.1.1. These distributions combined with added noise for each pixel leads to the distribution of ρ_{noise} values for no variation in tilt or coil angles.

Simulations were run with variable tilt angles and the resulting parameter ρ_{noise} is shown in figure 5.1. Figure 5.1a displays the resulting histograms from four simulations with θ_T from $0°$ to $60°$. Notice the shift towards higher values of the average of ρ_{noise} for higher tilt angles. These simulations represent straight fibrils cut at indicated tilt angles, in example tendon.

In addition four simulations were performed with θ_{T} normally distributed around a mean axis at $0°$ for varying standard deviance σ as shown in figure 5.1b. A simulation was also conducted with a completely uniform distribution of all possible θ_{T}. The results of the simulations are displayed as mean values and standard deviation of ρ_{noise}. These simulations, with varying degrees of disorder, should correspond to structures formed by collagen type II such as in cartilage.

Similar simulations were run with variable supercoil angles θ_{SC}, as shown in figure 5.2. They were performed in order to investigate whether or not any of the experimental samples produce similar distributions.

In figure 5.3, a simulation where both θ_{T} and θ_{SC} were modelled as normal distributions with mean $0°$ for standard deviations from $0°$ to $60°$. A simulation for uniform distributions in tilt and coil angles was also conducted and is represented by the green curve.

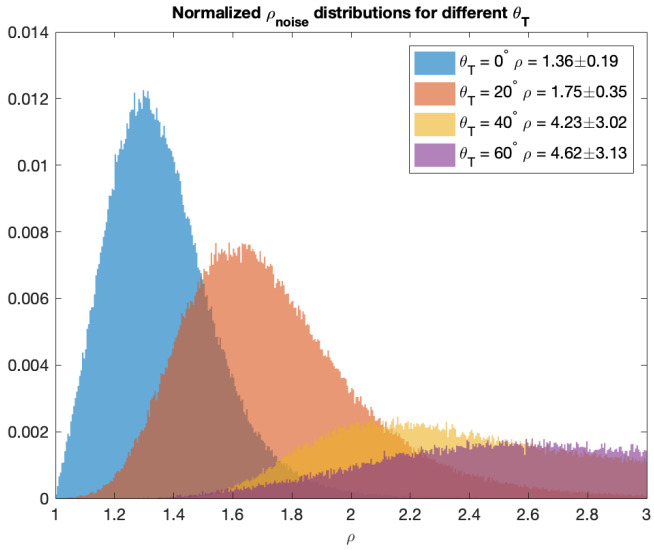

(a)

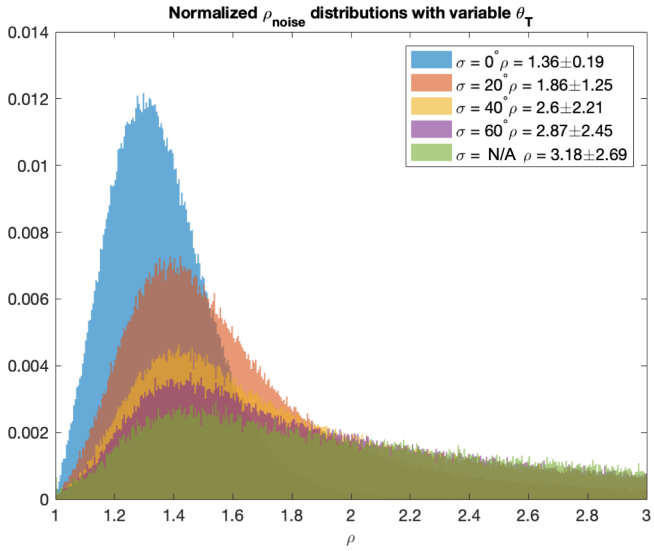

(b)

Figure 5.1: (**a**) Histograms of ρ_{noise} with helix angle $\theta_{\text{H}} = 53 \pm 1°$, triple helix angle $\theta_{3\text{H}} = 12 \pm 2°$ and tilt angles from 0° to 60° with 20° increments. (**b**) Histograms of ρ_{noise} with helix angle h $\theta_{\text{H}} = 53 \pm 1°$, triple helix angle $\theta_{3\text{H}} = 12 \pm 2°$ and normally distributed tilt angles with mean angle 0° and standard deviation σ from 0° to 60° with 20° increments. In addition, the green curve represents a completely uniform distribution with all tilt angles equally probable.

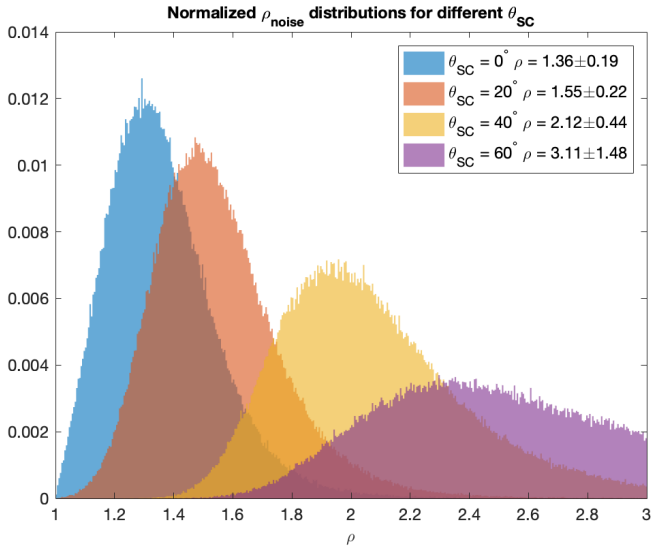

(a)

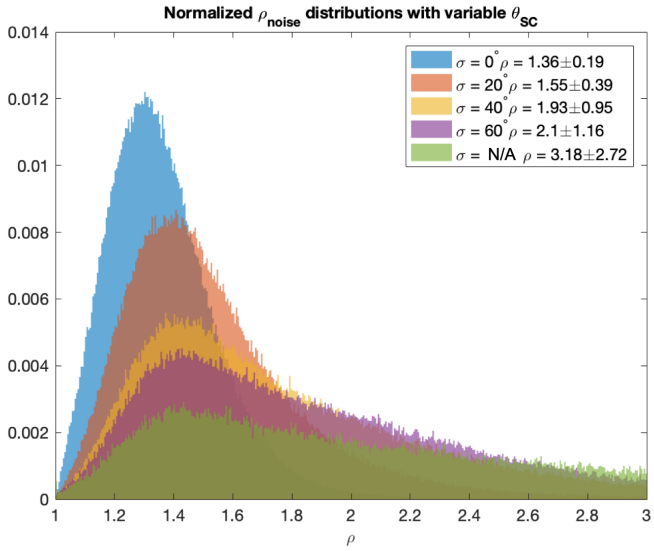

(b)

Figure 5.2: (**a**) Histograms of ρ_{noise} with helix angle $\theta_{\text{H}} = 53 \pm 1°$, triple helix angle $\theta_{3\text{H}} = 12 \pm 2°$ and supercoil angles θ_{SC} from 0° to 60° with 20° increments. (**b**) Normalized histograms of ρ_{noise} with helix angle h $\theta_{\text{H}} = 53 \pm 1°$, triple helix angle $\theta_{3\text{H}} = 12 \pm 2°$ and normally distributed supercoil angles with mean 0° and standard deviation σ from 0° to 60° with 20° increments. In addition, the green curve represents a completely uniform distribution with all supercoil angles equally probable.

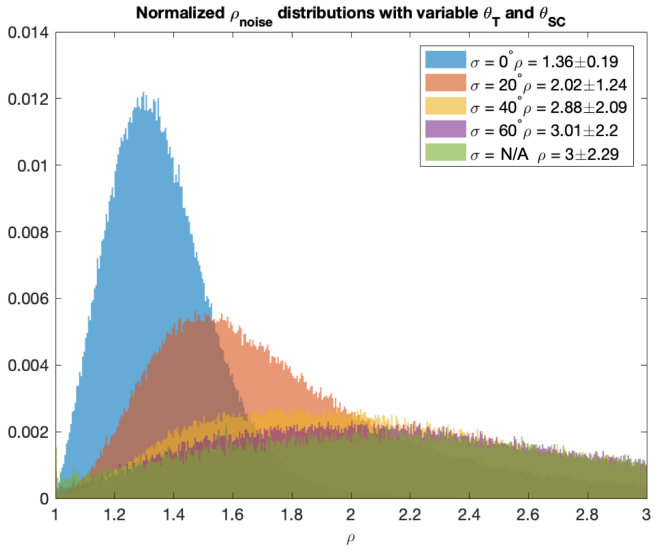

Figure 5.3: Histograms of ρ_{noise} with helix angle $\theta_{\text{H}} = 53 \pm 1°$ and triple helix angle $\theta_{3\text{H}} = 12 \pm 2°$. θ_T and θ_{SC} were modelled by normal distributions with mean 0° and standard deviations as indicated. The green curve represents uniform distribution in tilt and supercoil angles.

5.2 Experimental results

5.2.1 Chicken tendon

In order to verify the performed simulations, chicken tendon cut at both 20° and 30° was imaged. Additionally, since the cut angles and collagen structures of the tendon samples are known, they were used for picking the amount of shot noise applied to simulations.

The resulting histograms for ρ_{exp} for the chicken tendon samples cut at 20° and 30° are displayed in figure 5.4. In the first row, the calculated images of ρ_{exp} are displayed. The second row displays the resulting histogram for the tendon cut at 30° in addition to simulations for tilt angles θ_{T} from 0°-30°. Equivalent histograms for the tendon cut at 20° are displayed in the third row.

In figure 5.5, additional images of the tendon cut at 20° are displayed with their corresponding histograms. Notice that the images created from the main orientation angle γ appear to be fairly uniform.

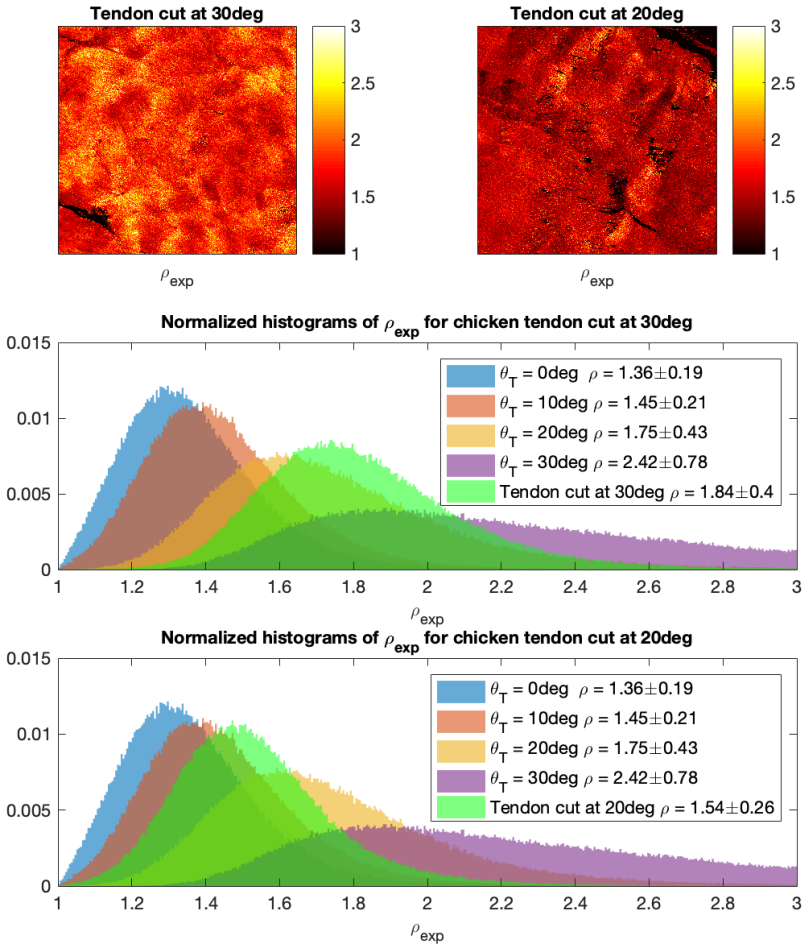

Figure 5.4: (First row) Displays calculated ρ_{exp} distributions of the chicken samples cut at 30° and 20°. **(Second row)** Normalized histograms of the sample cut at 30° overlaying histograms created by simulations with variable tilt angles. **(Third row)** Histograms of the sample cut at 20° overlaying histograms created by the aforementioned simulations.

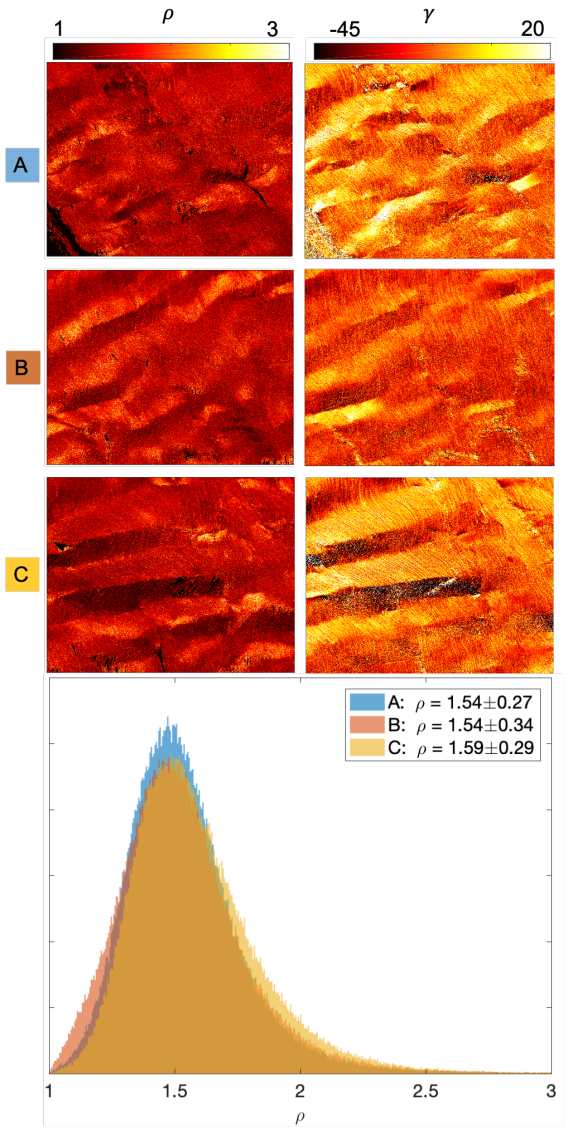

Figure 5.5: Three different regions of interest (ROI) for the chicken tendon sample. **(Left column)** Images depicting ρ for images A, and C. **(Right column)** Main angular orientation images γ for images A,B and C. **(Bottom)** Histograms illustrating ρ-distributions for images A,B and C. Mean and standard deviations are indicated.

5.2.2 Distal femur

In the following section, results from imaging of various parts of the pig knee joint are displayed. The overview tile scan of the sample is displayed in figure 5.6. The overview image reveals that the sample contains several types of tissue and they are highlighted for the purpose of illustration. Tendon seems to be present in 5.6A, 5.6B is bone while 5.6C is cartilage.

In total three similar knee joint samples from the same specimen were imaged and analyzed, but only one is illustrated. The main results from the samples are given in table 5.1.

In figure 5.7, images of four ROI are shown. The images are collected as a stack starting perpendicularly from the edge with evenly spaced $2.5\,\mathrm{mm}$ intervals. Images A,B and C consist of cartilage while image D consists of bone. The corresponding histograms are plotted on the lower left. The stack was imaged in order to see if P-SHG could detect any differences between different ROI in the cartilage area and the bone. Image A shows a high noise to signal ratio, explaining the discrepancy from histograms B, C and D.

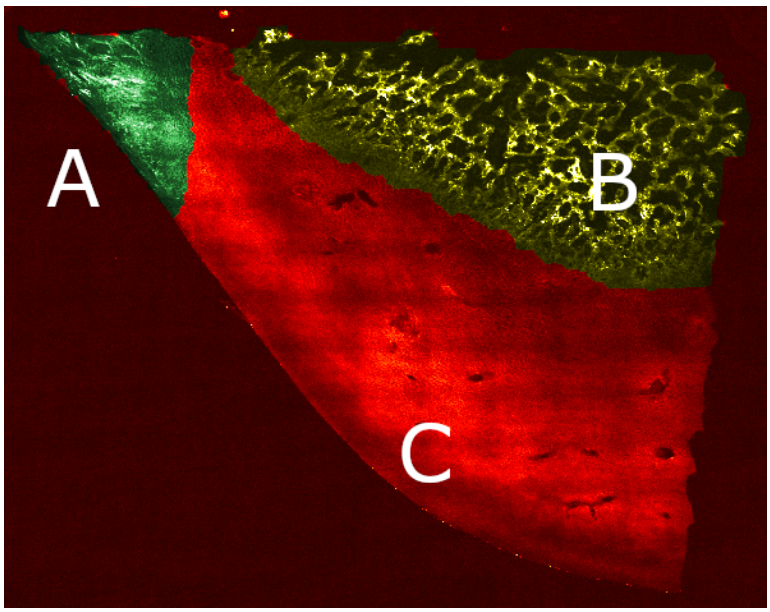

Figure 5.6: Tile SHG scan of the knee joint of a domestic pig. Three highlighted sections indicate different structures in the joint. **A** represents an area mainly consisting of tendon. **B** indicates an area mainly consisting of bone. **C** represents cartilage. The sections are colorized for the purpose of illustration.

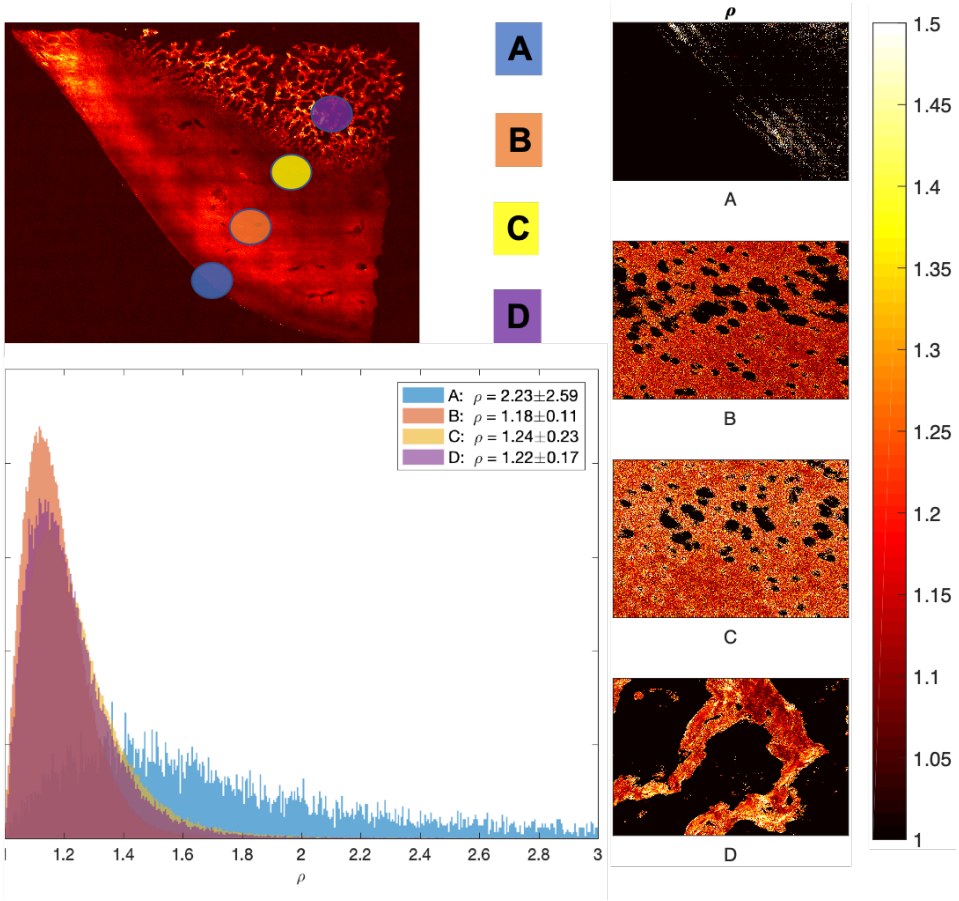

Figure 5.7: A stack of four ROI perpendicularly to the surface of the sample were imaged as indicated on the picture in the top left. The four ROI are displayed in addition to histograms of their ρ-distributions. Image A was taken on the edge of the sample, and the distribution indicates low signal strength. Images B and C are represent cartilage with a much stronger signal, while image D is bone.

Tendon

Figures 5.8 and 5.9 represent images from region A as shown in figure 5.6. In both figures, the region of interest is displayed in A. Images of $\rho_{\exp}$ calculated from the curve-fitting of the polarization images are shown in B. The pixel-resolved orientation angle γ is shown in C. Histograms are displayed in D for the calculated $\rho_{\exp}$ for both the signal measured in the forward (green curve) and the backward (red curve) direction.

In figure 5.10 similar curves are shown, but were imaged at the intersection between tendon and cartilage. Figure 5.10B indicates cartilage with parts of the image consisting mainly of tendon. Notice that several distinct sections oriented in different directions are clearly visible in the angular image.

In figure 5.11, different parts of figure 5.10 have been analyzed. Figure 5.11A shows the entire image, while B and C show tendon and the area around cartilage canals respectively. The histograms of each part were plotted in figure 5.11D.

Notice that for all images, $\rho_{\exp}$-distributions in the forward direction are more spread out than for the reflected direction.

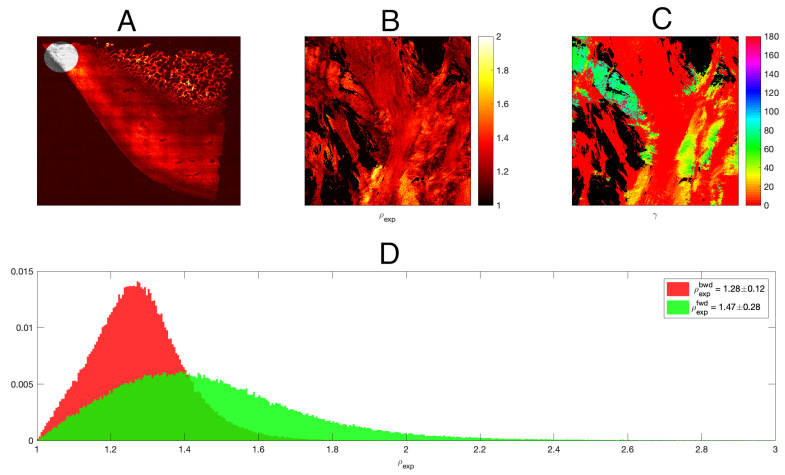

Figure 5.8: **A** Image of tendon from indicated area. **B** Image created from ρ_{exp} in the backwards direction. **C** Image of main angle γ in degrees. **D** Normalized 2D histograms displaying ρ_{exp} measured in both the forward (green curve) and backward direction (red curve). Mean values and standard deviations are displayed.

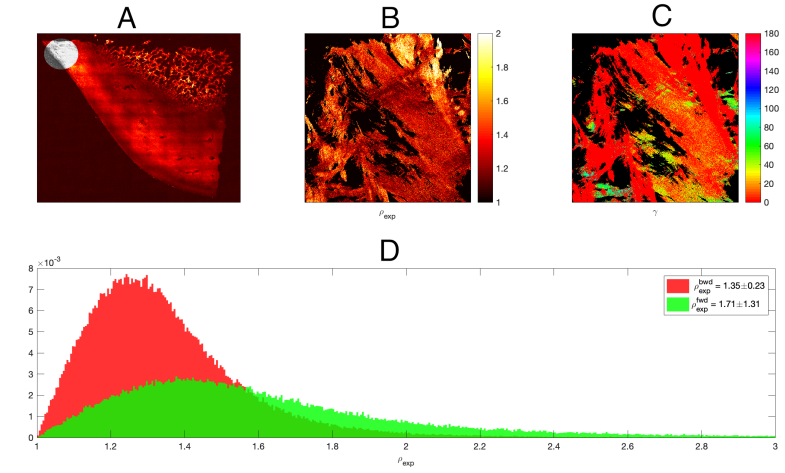

Figure 5.9: **A** Image of tendon from indicated area. **B** Image created from ρ_{exp} in the backwards direction. **C** Image of main angle γ in degrees. **D** Normalized 2D histograms displaying ρ_{exp} measured in both the forward (green curve) and backward direction (red curve). Mean values and standard deviations are displayed.

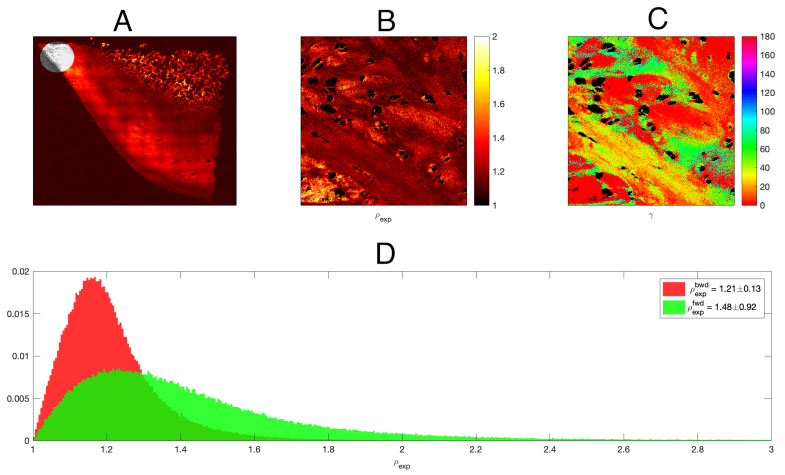

Figure 5.10: **A** Image of the transition between cartilage and tendon in indicated area. **B** Image created from ρ_{exp} in the backwards direction. **C** Image of main angle γ in degrees. **D** Normalized 2D histograms displaying ρ_{exp} measured in both the forward (green curve) and backward direction (red curve). Mean values and standard deviations are displayed.

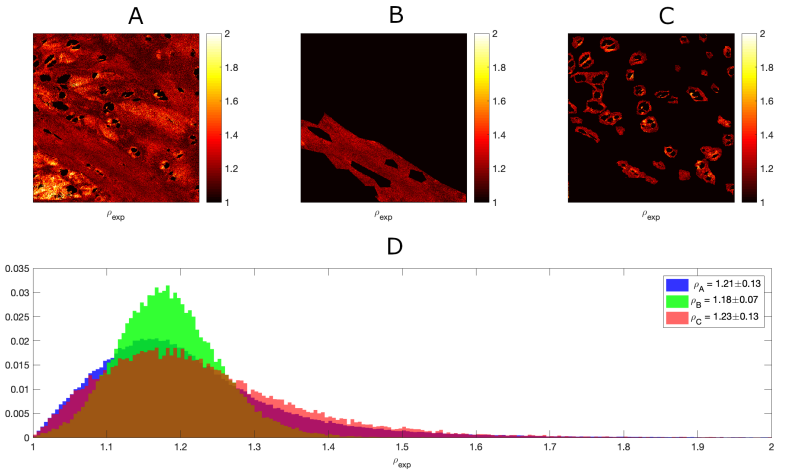

Figure 5.11: **A** Image of ρ_{exp} for the intersection between tendon and cartilage. **B** Region of interest of what is assumed to be tendon. **C** Region of interest of a thin membrane around the cartilage canals. **D** Normalized 2D histograms for A (blue curve), B (green curve) and C (red curve).

Cartilage

Figure 5.12 represents a polarization stack imaged in the region indicated in 5.12A. The cartilage canals indicated by black have been removed from the data. Figure 5.12B illustrates ρ_{exp} and shows a fairly homogeneous distribution which is not reflected by the main orientation angle distribution shown in figure 5.12C which is more heterogeneous. The distributions were found to be $\rho_{\mathrm{exp}} = 1.16 \pm 0.1$ for the reflected signal and $\rho_{\mathrm{exp}} = 1.57 \pm 1.34$ for the transmitted signal.

Two additional images of cartilage are displayed in figure 5.13. The images have been manipulated in order to separate the membranes surrounding the cartilage canals (b, d) from the rest of the ECM (a, c) with the purpose of investigating if the membranes can be used as a contrast mechanism. For (n = 3) regions of interest (ROI), the resulting mean values are $\rho_{\mathrm{MEM}} = 1.16 \pm 0.01$ and $\rho_{\mathrm{ECM}} = 1.18 \pm 0.01$.

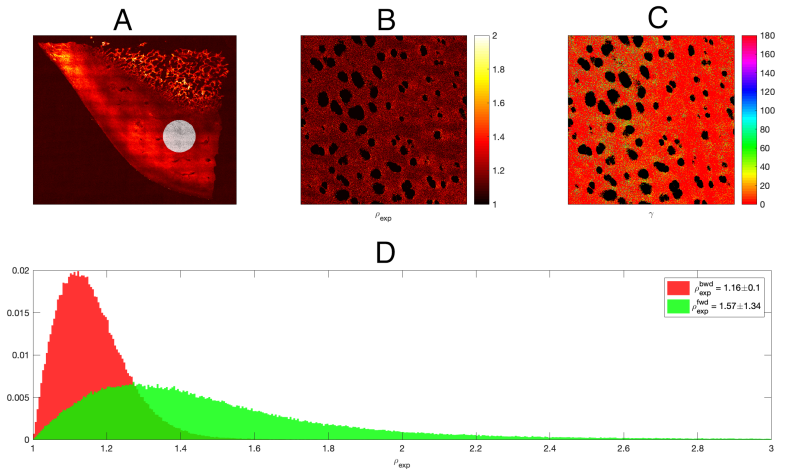

Figure 5.12: **A** SHG tile scan of a pig joint with a 10X objective. A region of interest is indicated with a grey circle. **B** Image of computed ρ_{exp} values. The image consists of 512x512 pixels from within the region of interest indicated in A. **C** Computed main orientation angles γ for the same image as in B. **D** Normalized 2D histograms for B detected in the forward direction (green curve) and in the reflected direction (red curve). $\rho_{\mathrm{exp}} = 1.16 \pm 0.1$

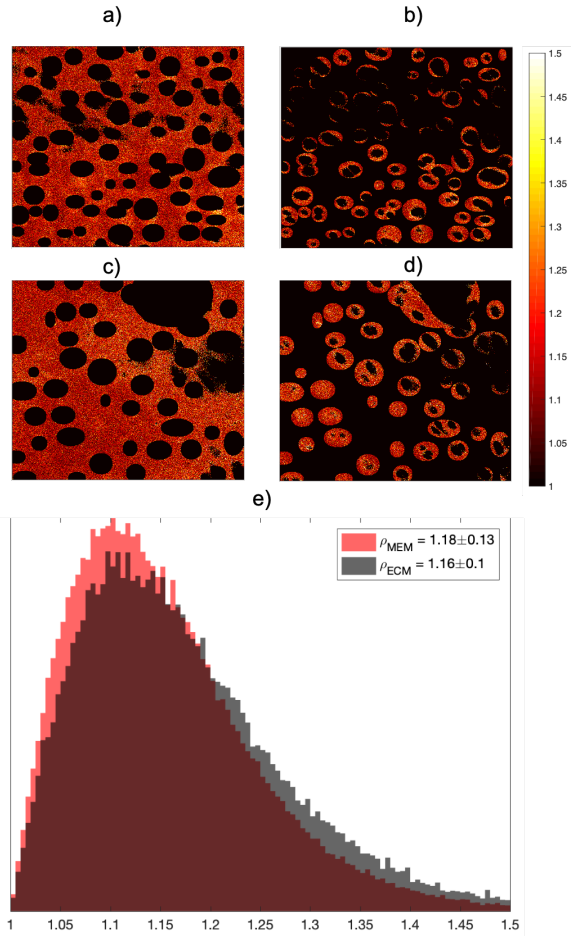

Figure 5.13: **(a, c)** Images of ρ for the ECM of two cartilage ROI. **(b, d)** Images of ρ for the membrane surrounding the cartilage canals for two cartilage ROI. **(e)** Histograms for $\rho_{\mathrm{MEM}}, \rho_{\mathrm{ECM}}$ corresponding to values of ρ for the membranes surrounding the cartilage canals and the rest of the ECM respectively.

Bone

Bone was assumed to be present in the region indicated by a grey circle in figure 5.14A. $\rho_{\exp}$ was calculated for each pixel from the reflected SHG stack and the results are displayed as an image in figure 5.14B. Similarly, the main orientation angle γ was calculated and is shown in figure 5.14C. Notice that γ is not as homogeneous as for tendon, but not as disorganized as for cartilage. Normalized histograms in the transmitted and reflected directions were found to be $\rho_{\exp} = 1.51 \pm 0.4$ and 1.24 ± 0.25 respectively.

In order to investigate whether it is possible to utilize polarization resolved SHG in order to differentiate between cartilage and bone, the intersection between the two cases was imaged in figure 5.15. The image was then split into two sections at the apparent interface with the cartilage and bone illustrated in figures 5.15B and 5.15C. The normalized histograms for the images A,B and C are displayed in figure 5.15D, and are shown to be $\rho_{\exp} = 1.22 \pm 0.2$ and 1.24 ± 0.24 for cartilage and bone respectively.

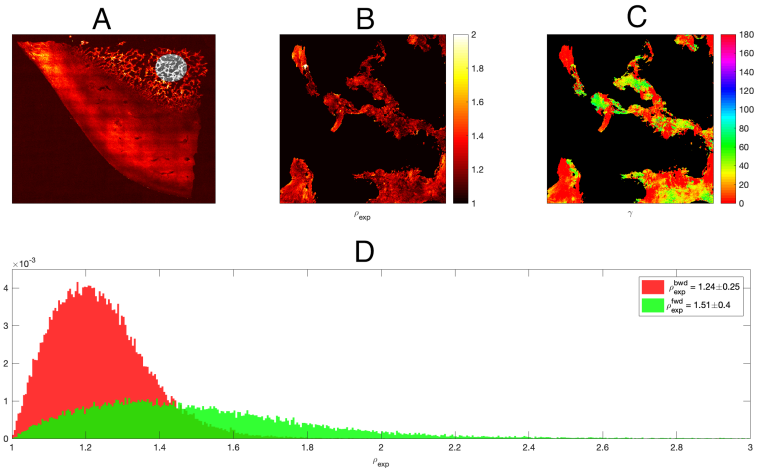

Figure 5.14: **A** SHG tile scan of a pig joint with a 10X objective. A region of interest in the area assumed to be bone is indicated with a grey circle. **B** Image of computed $\rho_{\exp}$ values. The image consists of 512x512 pixels from within the region of interest indicated in A. **C** Computed main orientation angles γ for the same image as in B. Notice that North is 0 degrees. **D** Normalized 2D histograms for B detected in the forward direction (green curve) and in the reflected direction (red curve). $\rho_{\exp} = 1.24 \pm 0.25$

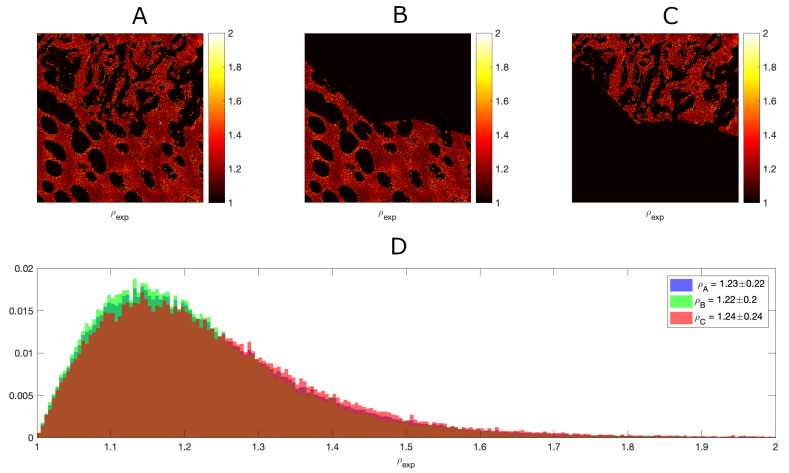

Figure 5.15: **A** SHG polarization stack $\rho_{\exp}$ image of the interface between bone and cartilage in a pig joint. **B** Section of image assumed to be cartilage. **C** Section of image assumed to be bone and cartilage. **D** Normalized 2D histograms for the interface A (blue curve), the cartilage section B (green curve) and the bone/cartilage section C (red curve). Notice the negligible difference.

Table 5.1: Results from analysis of the pig knee joint. Standard deviation represents standard deviation computed from an array of all data points from bone, tendon or cartilage.

Tissue	Bone	Tendon	Cartilage
ρ_{exp}	1.25	1.25	1.22
Std ρ_{exp}	0.25	0.34	0.22
n	6	7	11

Chapter 6

Discussion

This chapter will start with an evaluation of the simulation model of collagen structures. Then, the investigated samples are discussed separately. Finally, the initial goal of separating between collagen structures and consequently collagen types is discussed in addition to other findings and encountered anomalies.

6.1 Simulations

Several simulations were run in order to test the implementation of the model created by Rouede et al [1]. Attempts at modelling experimental results by variation of the model input angles were done. It is important to note that the model has not been tested for cartilage before. However, it has been tested extensively for tendon which is used as a validation of the model implementation in the following section.

6.1.1 Simulating tendon

Tendon was simulated as straight fibrils with no tilt angle disorder ($\sigma = 0$) and no variation in other parameters, in agreement with previous studies [1, 23, 11, 8, 19]. The results are presented in figure 5.1a. Note that disorder in ρ_{noise} is increasing with higher tilt angles. It is also worth noting that these histograms were created by applying shot noise to the simulated intensity curves for each pixel. The noise level was chosen based on the best match with curves made from images with *a priori* known tilt angles. The curves are in agreement with previous simulations made by Rouede [8] and by Romijn [23].

6.1.2 Simulating cartilage

The following cases represent various degrees of disorder. The idea is that the level of disorder can be determined by comparing the following simulations with experimental data for cartilage. As for tendon, all attempts at simulating cartilage were done with a shot

noise level found by fitting the simulated distributions to histograms found for chicken tendon and then choosing the best fitting noise level.

Tilt angle

An original assumption in this thesis was that structures such as tendon or bone are characterized by approximately straight fibrils while the fibrils in cartilage are distributed with a higher degree of disorder. In order to try to simulate cartilage, a standard deviation in θ_{T} was introduced as shown in figure 5.1b. It is worth noting that introducing a variation in the tilt angle has approximately the same effect as introducing a higher level of shot noise. This leads to further room for error when attempting to use P-SHG images for determination of collagen structures as it is another parameter that must be known *a priori*.

Supercoil angle

Additionally, a fixed supercoil angle was introduced as shown in figure 5.2a. This represents undulation of the fibrils with a fixed angle, making the coil constant. Notice that the resulting histograms are not identical, but show the same behaviour as for the tilt angle case. This follows from the matrix equation in section 3.1, where both the supercoil and tilt levels are modelled similarly.

It is also possible that the undulation angles in the fibrils can vary between pixels and this is simulated in figure 5.2b. Finally, a case of disorder in both tilt and supercoil angles was investigated. In figure 5.3, histograms are shown for varying degrees of disorder in both parameters.

As seen in figures 5.4 and 5.1b, an increase in tilt or coil angle disorder leads to a shift in the mean of ρ to higher values. The model does not seem to be capable of creating distributions with a mean value lower than 1.36 at the current choice of shot noise. It can be seen from figure 4.3a that if the signals are not rendered noisy, straight fibrils with no disorder or undulations result in mean value $\rho_{\mathrm{noise}} = 1.28$.

6.2 Chicken tendon

Images formed by the processing routine explained in section 4.4.1 are displayed in figure 5.4. In the second and third rows, the histograms of the ρ_{exp} distributions are plotted with the simulated distributions for tendon cut at tilt angles between 0°-30°.

The simulations were calibrated with a shot noise level to match the experimental data. The tendon cut at 30° with $\rho = 1.84 \pm 0.4$ seems to approximately fit the simulation for $\theta_{\mathrm{T}} = 20°$ with $\rho = 1.75 \pm 0.43$. Similarly, the simulation for $\theta_{\mathrm{T}} = 10°$ with $\rho = 1.45 \pm 0.21$ fits the distribution calculated from the tendon sample cut at 20° with $\rho = 1.54 \pm 0.26$.

The simulations could possibly be run for a slightly higher tilt angle for both cases in order to provide even better matches, but generally the experimental data confirms the validity of the simulations. The deviation between experimental and simulated data could be a result of inaccurate cutting of the sample as a 5°-10° difference is negligible.

6.3 Pig knee joint

In the following section, several regions of interest in the distal femur of a sus scrofa are investigated. The result of the tile scan of the sample is displayed in figure 5.6. As the sample contains roughly three different sections, with different concentrations of collagen, there was a difficulty achieving sufficient contrast to be able to illustrate the entire sample. The tendon and bone sections resulted in a high signal, while parts of the collagen section were almost invisible in comparison. Therefore, the noise in the image was decreased using an averaging filter over 3×3 pixels.

It is also worth mentioning that the tile borders are observable on the image, which is caused by some of the tiles overlapping. The image does however fulfill the purpose of illustration.

6.3.1 Tendon

In figure 5.8 one ROI from the tendon section of the sample as shown in A. The effective orientation angle γ shows that most pixels are oriented north-south, which is especially obvious in the middle of image C. The reflected mean value of $\rho_{\exp} = 1.28 \pm 0.12$ supports this as it is similar to simulations run for low tilt angles, see figure 5.1a.

This is further confirmed by the pixels in figure 5.9C, which show a tendency of having main orientation angles slightly tilted, but also with a higher mean value of $\rho_{\exp} = 1.35 \pm 0.23$. This is also in agreement with simulations for tendon.

In both figures, the signal collected in the forwards direction is also presented with similar histograms. Notice that the histograms for the forwards direction consistently show higher standard deviations for $\rho_{\exp}$.

6.3.2 Bone

Several ROI of the bone section was imaged (n=5) and the resulting $\rho_{\exp} = 1.27 \pm 0.27$ is shown in table 5.1. One of these images is displayed in figure 5.14 showing a histogram similar to those found for tendon. The initial assumption was that bone would be more ordered than cartilage and characterized by thick fibrils. The histograms calculated for bone are similar to those for tendon.

6.3.3 Cartilage

Surprisingly, cartilage showed a remarkably uniform distribution of effective angle γ, with a main orientation angle average of approximately 20°, as can be seen in figure 5.12. The ρ-distribution has a mean value of $\rho_{\exp} = 1.16 \pm 0.1$ which is lower than for tendon. In total, 9 ROI in cartilage on three slices of the same distal femur were imaged. As can be seen in table 5.1, $\rho_{\exp} = 1.22 \pm 0.22$ for cartilage, which is not in agreement with simulations if the original assumption of cartilage being more disordered than tendon is valid.

6.3.4 Areas of transition

It should now be clear that using $\rho_{\exp}$ as a method of distinguishing between collagen structures such as bone, tendon and cartilage, or equivalently collagen types I and II is proving difficult. The intersection between tendon and cartilage in one of the distal femur samples was examined, see figure 5.11. In figure (5.11A), both tendon and cartilage can be observed. An attempt to separate the pixels only containing the tendon was made, see figure (5.11B). The two histograms are compared in figure (5.11) providing values $\rho_{\exp} = 1.21$ and $\rho_{\exp} = 1.18$ respectively. No significant difference is observed.

The transitional area between cartilage and bone was also investigated, see figure 5.15. The image was divided into two parts, one believed to be bone and another cartilage. The histograms overlap and there seems to be no difference of significance.

6.3.5 Investigation of cartilage canals

Mansfield et al [24] suggested that fibrils close to the canals in cartilage could provide different histograms as compared to the rest of the ECM. An attempt was made to investigate this possibility, see figure (5.11C). Interestingly, there is a difference between the ρ-distributions around the cartilage canals and elsewhere. The fibrils around the cartilage canals consistently show higher values of ρ. However, it can not be used as a contrast mechanism in order to separate between collagen types I and II, because both values overlap with results from both bone and tendon.

Further work could be done by investigating if there is a depth-variation between the membranes around the cartilage canals. The fibrils around the cartilage canals could potentially be used as a new contrast mechanism, but a larger sample size is required to confirm the results.

6.3.6 Discrepancy between transmitted and reflected signal

It is evident from the results that there is a significant difference between $\rho_{\exp}$ distributions calculated from signals measured in the forward and backward directions, see for example figures 5.9 and 5.10. A key find is that when comparing to signals from tendon samples in the forward direction, the calculated $\rho_{\exp}$ distributions can be simulated by a weaker signal or by equivalently applying more noise, which indicates that the signal collected in the forward direction is subject to more noise than the reflected signal.

This could be due to a difference in detectors, the PMT-detector used to image in the forward direction could be more susceptible to shot noise when compared to the HyD-detector used for reflected imaging.

Another possible reason is that the imaging was performed on relatively thick samples ($50\,\mu\mathrm{m}$). Hence it is possible that the transmitted signal was scattered passing through the thick sample before reaching the PMT-detector.

6.3.7 Distinguishing between collagen structures

From the data given in table 5.1, it is evident that according to the P-SHG data there is no significant difference between the collagen structures in cartilage, tendon and bone. There

is a lot of variation of mean values of ρ even inside the same sample, which is larger than between structures. It does seem like ρ can not be used to provide any further contrast in the case of (sus scrofa) bone, tendon and cartilage.

It is possible that on a much smaller scale than the resolution of the optical system used in this thesis, the cartilage is close to randomly oriented as indicated by electron microscopy [25]. On the scale of the optical point spread function used in this experiment, it is evident that the fibrils in cartilage are ordered.

6.3.8 Comparison with simulations

Referring to 5.1, there is no significant difference in ρ-distributions between collagen structures and by extension collagen types, indicating that simulations for tendon also correspond to cartilage and bone. In addition, the model does not seem to be able to simulate ρ-distributions with mean values as low as those found in the distal femur (see section 5.1).

Cartilage can not be simulated by any level of disorder in tilt angle or supercoil angle. The initial assumption of cartilage being characterized by a higher level of disorder hence does not agree with simulations, indicating that the model needs further improvement. It does however sufficiently simulate chicken tendon, as confirmed for two cut angles.

Chapter 7

Conclusion

In this thesis an existing method of simulating the second order optical susceptibility of collagen fibrils was implemented, analyzed and utilized in an attempt to classify collagen structures based on *a priori* known information about their composition. In order to do this, ρ was calculated for both simulated collagen structures and P-SHG images. Tendon extracted from a chicken knee joint was successfully simulated as straight fibrils. This verifies the model for two different cut angles. The result was used in order to calibrate the shot noise level of the simulation model for the microscope settings used in the experiment.

Any attempt at distinguishing between collagen structures in the pig knee joint through ρ as a contrast mechanism was unsuccessful, even with applied noise. However, this needs further confirmation through expanding the experiment to different specimen with a larger sample size. Consequently, simulating cartilage was proven difficult as the measurements were not significantly different from those for tendon. Furthermore, attempts at investigating fibrils around cartilage canals and the rest of the ECM failed at being a useful method of contrast, but should be investigated further as there was a consistent difference between the cartilage canals and the ECM.

Bibliography

[1] Denis Rouède, Emmanuel Schaub, Jean-Jacques Bellanger, Frédéric Ezan, Jean-Claude Scimeca, Georges Baffet, and François Tiaho. Determination of extracellular matrix collagen fibril architectures and pathological remodeling by polarization dependent second harmonic microscopy. *Scientific reports*, 2017.

[2] Gloria A Di Lullo, Shawn M Sweeney, Jarmo Körkkö, Leena Ala-Kokko, and James D San Antonio. Mapping the ligand-binding sites and disease-associated mutations on the most abundant protein in the human, type i collagen. *Journal of Biological Chemistry*, 2002.

[3] B Ytrehus, Cathy S Carlson, and S Ekman. Etiology and pathogenesis of osteochondrosis. *Veterinary pathology*, 2007.

[4] François Tiaho, Gaëlle Recher, and Denis Rouède. Estimation of helical angles of myosin and collagen by second harmonic generation imaging microscopy. *Optics express*, 2007.

[5] Adam E Tuer, Margarete K Akens, Serguei Krouglov, Daaf Sandkuijl, Brian C Wilson, Cari M Whyne, and Virginijus Barzda. Hierarchical model of fibrillar collagen organization for interpreting the second-order susceptibility tensors in biological tissue. *Biophysical journal*, 2012.

[6] Patrick Christian Stoller, Beop-Min Kim, Alexander M Rubenchik, Karen M Reiser, and Luiz Barroca Da Silva. Polarization-dependent optical second-harmonic imaging of rat-tail tendon. *Journal of biomedical optics*, 2002.

[7] Xiyi Chen, Oleg Nadiarynkh, Sergey Plotnikov, and Paul J Campagnola. Second harmonic generation microscopy for quantitative analysis of collagen fibrillar structure. *Nature protocols*, 2012.

[8] Denis Rouede, Emmanuel Schaub, Jean-Jacques Bellanger, Frédéric Ezan, and François Tiaho. Accordion-like collagen fibrils suggested by p-shg image modeling: implication in liver fibrosis.

[9] Matthew D. Shoulders and Ronald T. Raines. Collagen structure and stability. *Annual review of biochemistry*, 2009.

[10] Achilleas D Theocharis, Spyros S Skandalis, Chrysostomi Gialeli, and Nikos K Karamanos. Extracellular matrix structure. *Advanced drug delivery reviews*, 2016.

[11] Karl E Kadler, David F Holmes, John A Trotter, and John A Chapman. Collagen fibril formation. *Biochemical Journal*, 1996.

[12] DR Eyre, J-J Wu, RJ Fernandes, TA Pietka, and MA Weis. Recent developments in cartilage research: matrix biology of the collagen ii/ix/xi heterofibril network, 2002.

[13] Riccardo Gottardi, Uwe Hansen, Roberto Raiteri, Marko Loparic, Marcel Düggelin, Daniel Mathys, Niklaus F Friederich, Peter Bruckner, and Martin Stolz. Supramolecular organization of collagen fibrils in healthy and osteoarthritic human knee and hip joint cartilage. *PloS one*, 2016.

[14] S. Fine and W. P. Hansen. Optical second harmonic generation in biological systems. 1971.

[15] Robert W Boyd. *Nonlinear optics*. Elsevier, 2003.

[16] G Wagniere. Theoretical investigation of kleinman symmetry in molecules. *Applied Physics B*, 1986.

[17] Sergey V Plotnikov, Andrew C Millard, Paul J Campagnola, and William A Mohler. Characterization of the myosin-based source for second-harmonic generation from muscle sarcomeres. *Biophysical journal*, 2006.

[18] Ivan Amat-Roldan, Sotiris Psilodimitrakopoulos, Pablo Loza-Alvarez, and David Artigas. Fast image analysis in polarization shg microscopy. *Optics express*, 2010.

[19] Denis Rouède, Jean-Jacques Bellanger, Jérémy Bomo, Georges Baffet, and François Tiaho. Linear least square (lls) method for pixel-resolution analysis of polarization dependent shg images of collagen fibrils. *Optics Express*, 2015.

[20] Olena S Rabotyagova, Peggy Cebe, and David L Kaplan. Collagen structural hierarchy and susceptibility to degradation by ultraviolet radiation. *Materials Science and Engineering: C*, 2008.

[21] Shi-Wei Chu, Szu-Yu Chen, Gia-Wei Chern, Tsung-Han Tsai, Yung-Chih Chen, Bai-Ling Lin, and Chi-Kuang Sun. Studies of χ (2)/χ (3) tensors in submicron-scaled bio-tissues by polarization harmonics optical microscopy. *Biophysical journal*, 2004.

[22] MATLAB. *Version 9.2 (R2017a)*. The MathWorks Inc., Natick, Massachusetts, 2017.

[23] Elisabeth I Romijn, Andreas Finnøy, and Magnus B Lilledahl. Analyzing the feasibility of discriminating between collagen types i and ii using polarization-resolved second harmonic generation. *Journal of biophotonics*, 2019.

[24] Jessica C Mansfield, Vipul Mandalia, Andrew Toms, C Peter Winlove, and Sophie Brasselet. Collagen reorganization in cartilage under strain probed by polarization sensitive second harmonic generation microscopy. *Journal of the Royal Society Interface*, 2019.

[25] A Changoor, M Nelea, S Méthot, N Tran-Khanh, A Chevrier, A Restrepo, MS Shive, CD Hoemann, and MD Buschmann. Structural characteristics of the collagen network in human normal, degraded and repair articular cartilages observed in polarized light and scanning electron microscopies. *Osteoarthritis and Cartilage*, 2011.

Appendix

```
%Calculating x33/x31/rho from a given set of angles. Inputs are arrays of
%angles, ie. a gaussian/uniform distribution in radians.

function [rho, x33, x31] = rhoth(thetaT,thetaSC, thetaH, theta3H, phiT, phiSC, beta)
for i = 1:length(thetaT)
    mat1 = [cos(thetaT(i))^2 3*sin(thetaT(i))^2;cos(phiT(i))^2*sin(thetaT(i))^2 1-3*cos(phiT(i))^(2)*sin(thetaT(i))^2];
    mat2 = [cos(thetaSC(i))^2 3*sin(thetaSC(i))^2;mean(cos(phiSC)^2)*sin(thetaSC(i))^2 1-3*mean(cos(phiSC)^2)*sin(thetaSC(i))^2];
    mat3 = [cos(theta3H(i))^2 3*sin(theta3H(i))^2;0.5*sin(theta3H(i))^2 1-1.5*sin(theta3H(i))^2];
    mat4 = [cos(thetaH(i))^2 3*sin(thetaH(i))^2;0.5*sin(thetaH(i))^2 1-1.5*sin(thetaH(i))^2];
    mat5 = [beta; 0];

    chi = cos(thetaT(i))*cos(thetaSC(i))*cos(theta3H(i))*cos(thetaH(i))*mat1*mat2*mat3*mat4*mat5;

    rho(i) = chi(1)/chi(2);
    x33(i) = chi(1);
    x31(i) = chi(2);
end
end
```

```
%%%Input sets of x31 and x33 created from rhoth


function [rho,a,b,c, phi, theta,I] = noise(x31,x33)
alpha=[0:20:160]; % adjust if not used with 9 polarization angles at interval 0:20:160
K = 1000; %Amplitude of Intensity I. Adjust in order vary noise level
I = zeros(length(x31),length(alpha));
%%%Simulated intensity curve
for i = 1:length(x31)
    %Looping through all x31/x33 for all angles
for j = 1:length(alpha)
```

```
    I(i,j) =K*(x31(i)*sind(2*alpha(j))^2 + (x31(i)*sind(
        alpha(j))^2 + x33(i)*cosd(alpha(j))^2)^2);
end
end
alpha = transpose(alpha);
I = transpose(I);
%%%Applying noise through matlab's poissrnd
for i = 1:length(x31)
    Ipoiss(:,i) = poissrnd(I(:,i));
end
%Removing potential negative values
Ipoiss(I<0) = NaN;
%Recalculating new x31, x33 values
for i = 1:length(x31)
    [x1(i),x2(i), c(i),phi(i),theta(i)] = LLSfit(Ipoiss(:,i
        ),alpha);
    rhopoiss(i) = x2(i)/x1(i);
     if x1(i) < 10^5 %%remove low values of x1 due to
         rounding errors
         rhopoiss(i) = NaN;
     end
end
rho = rhopoiss;
a = x1;
b = x2;
end
```

```
%%Function creating angular distributions
function [thetaT, thetaH, theta3H, thetaSC, phiT, phiSC,
    phiSCmean] = createdist(muT, sigmaT, muH, sigmaH, mu3H,
    sigma3H,muSC,sigmaSC,muPhiT,sigmaPhiT,muPhiSC,sigmaPhiSC
    )
N = 512*512; %Number of simulations ( pixels )
pdT = makedist('Normal',muT,sigmaT);
pdH = makedist('Normal',muH,sigmaH);
pd3H = makedist('Normal',mu3H,sigma3H);
pdSC = makedist('Normal',muSC,sigmaSC);
pdPhiSC = makedist('Normal',muSC,sigmaSC);
pdPhiT = makedist('Normal',muPhiT,sigmaPhiT);

thetaT = random(pdT,N,1)*pi/180;
thetaH = random(pdH,N,1)*pi/180;
theta3H = random(pd3H,N,1)*pi/180;
thetaSC = random(pdSC,N,1)*pi/180;

phiT = rand(1,N)*pi;
```

```
17
18 phiSC = rand(1,N)*pi;
19 phiSCmean = mean(phiSC);
20
21 end
```

```
1  clear;
2  beta = 1;
3  N = 512*512; % pixels
4  %Set chosen mean angles and standard deviations
5  muT = 0;
6  sigmaT = 0.001;
7  muH = 53;
8  sigmaH = 0.001;
9  mu3H = 12;
10 sigma3H = 0.001;
11 muSC = 0;
12 sigmaSC = 0.001;
13
14 muPhiT = 0;
15 sigmaPhiT = 0.001;
16
17 muPhiSC = 0;
18 sigmaPhiSC = 0.001;
19 %creating angle distributions
20 [thetaT, thetaH, theta3H, thetaSC, phiT, phiSC, phiSCmean]
       = createdist(muT, sigmaT, muH, sigmaH, mu3H,sigma3H,muSC
       ,sigmaSC,muPhiT,sigmaPhiT,muPhiSC,sigmaPhiSC);
21 [rho,x33,x31] = rhoth(thetaT,thetaSC,thetaH,theta3H,phiT,
       phiSCmean,beta);
22 [rho2, a, b, c, phi, theta] = noise(x31,x33); % Application
        of noise
```

```
1  %%Importing P-SHG stack and calibrating for intensity
       variations
2  function [polimage,realimage, alpha] = imageimp(filepath,
       filename)
3  alpha = [0:20:160];
4  calibration = [1.00 1.04 1.10 1.15 1.17 1.12 1.09 1.03
       0.99];
5  for i = 1:9
6      k = alpha(i);
7      image = imread(strcat(filepath,filename,num2str(i),'
           _ch01.tif'));
8      image = image(:,:,2) + image(:,:,1) + image(:,:,3);
9      polimage(:,:,i) = double(image)./calibration(i);
```

```
    realimage(:,:,i) = double(image)./calibration(i);
end
polimage = permute(polimage,[3 2 1]);
polimage = polimage(:,:);
polimage = permute(polimage, [2, 1]);
polimage = transpose(polimage);
polimage = polimage.*(polimage>=0);
alpha = transpose(alpha);
end
```

```
%Input generated or measured intensity curves and an array containing
%polarization angle.

function [a,b,c,phi,theta] = LLSfit(I, alpha)
A = ones(size(alpha));

Q = [A cosd(2*alpha) sind(2*alpha) cosd(4*alpha) sind(4*alpha)];
C = inv(transpose(Q)*Q)*transpose(Q)*I;

R1 = sqrt((C(2)^2 + C(3)^2)/(C(1)^2));
R2 = sqrt((C(4)^2 + C(5)^2)/(C(1)^2));

a = sqrt(2)*(((1+3*R2)/(1-R2-R1) - sqrt((1-R2+R1)/(1-R2-R1)))^(-1/2));
b = sqrt(2)*(((1+3*R2)/(1-R2+R1) - sqrt((1-R2-R1)/(1-R2+R1)))^(-1/2));
X31 = a; X33 = b;

c = 8*C(1)/(4+3*(a^2)+3*(b^2)+2*a*b);
theta = acosd(sqrt(b/(2+b)));
phi = rad2deg(0.5*angle(C(2)+1i*C(3)));
end
```

```
%Function calculating rho and angular distributions from P-SHG stack

function [] = calculateparameters(threshold, filepath, filename, outputpath, outputname)
[intensity,realimage,alpha] = imageimp(filepath,filename); %importing stack
intensity(10,:) = intensity(1,:);
check = intensity;
alpha = [0:20:180];
alpha = transpose(alpha);
```

```
tempimg = zeros(512,512);
for j = 1:9
    tempimg = tempimg + realimage(:,:,j);
end
tempimg(tempimg<0) = 0;
intensity(intensity<0) = 0;
for i = 1:length(intensity(1,:))
[a,b,c,phi,theta] = LLSfit(intensity(:,i), alpha);
rho(i) = abs(b)/abs(a);
clog(i) = c;
thetavec(i) = theta;
a1(i) = abs(a);
b1(i) = real(b);
phivec(i) = phi;
end
rho = vec2mat(rho,512);
rho = rho.*(tempimg(:,:)>=threshold);
rho = transpose(rho);
realimage2 = tempimg.*(tempimg(:,:)>=threshold);
tempphi = vec2mat(phivec,512);
phivec2 = tempphi.*(tempimg(:,:)>=threshold);
phivec2 = transpose(phivec2);
phivec2 = phivec2(:);
temptheta = vec2mat(thetavec,512);
thetavec2 = temptheta.*(tempimg(:,:)>=threshold);
thetavec2 = transpose(thetavec2);
thetavec2 = thetavec2(:);
rho(rho==0) = NaN;
phivec2(phivec2==0) = NaN;
thetavec2(thetavec2==0) = NaN;
figure %displaying histogram of rho
histogram(rho,10000);
xlim([0,3]);
intensity = double(intensity);
figure %displaying image
imagesc(tempimg);
figure
tempimg(tempimg<threshold) = 0;
imagesc(tempimg);
colorbar;

save([outputpath outputname '.mat'], 'rho', 'phivec', 'a','
    clog','realimage2','phivec2','thetavec2');
end
```